Modeling extreme precipitation over East China with a global variable-resolution modeling framework (MPASv5.2): Impacts of resolution and physics

[1]Chun Zhao, [1]Mingyue Xu, [1]Yu Wang*, [1]Meixin Zhang, [2]Jianping Guo, [3]Zhiyuan Hu, [4]L. Ruby Leung, [5]Michael Duda, [5]William Skamarock

[1]School of Earth and Space Sciences, University of Science and Technology of China, Hefei, China

[2]State Key Laboratory of Severe Weather, Chinese Academy of Meteorological Sciences, Beijing, China

[3]Key Laboratory for Semi-Arid Climate Change of the Ministry of Education, Lanzhou University, Gansu, China

[4]Atmospheric Sciences and Global Change Division, Pacific Northwest National Laboratory, Richland, WA, USA

[5]National Center for Atmospheric Research, Boulder, CO, USA

Manuscript for submission to Geoscientific Model Development

*Corresponding authors: Yu Wang (wangyu09@ustc.edu.cn)

Key points:

1. MPAS simulations at global uniform and variable resolutions share similar characteristics of precipitation and wind in the refined region.
2. Numerical experiments reveal significant impacts of resolution on simulating the distribution and intensity of precipitation and updrafts.
3. Study provides evidence supporting the use of convection-permitting global variable-resolution simulation for studying extreme precipitation.

Abstract

The non-hydrostatic atmospheric Model for Prediction Across Scales (MPAS-A), a global variable-resolution modeling framework, is applied at a range of resolutions from hydrostatic (60 km, 30 km, 16 km) to non-hydrostatic (4 km) scales using regional refinement over East Asia to simulate an extreme precipitation event. The event is triggered by a typical wind shear in the lower layer of the Meiyu front in East China during 25-27 June 2012 of the East Asian summer monsoon season. The simulations are evaluated using ground observations and reanalysis data. The simulated distribution and intensity of precipitation are analyzed to investigate the sensitivity to model configuration, resolution, and physics parameterizations. In general, simulations using global uniform-resolution and variable-resolution meshes share similar characteristics of precipitation and wind in the refined region with comparable horizontal resolution. Further experiments at multiple resolutions reveal the significant impacts of horizontal resolution on simulating the distribution and intensity of precipitation and updrafts. More specifically, simulations at coarser resolutions shift the zonal distribution of the rain belt and produce weaker heavy-precipitation centers that are misplaced relative to the observed locations. In comparison, simulations employing 4 km cell spacing produce more realistic features of precipitation and wind. The difference among experiments in modeling rain belt features is found mainly due to the difference of simulated wind shear formation and evolution during this event. Sensitivity experiments show that cloud microphysics have significant effects on modeling precipitation at non-hydrostatic scales, but their impacts are relatively small compared to that of convective parameterizations for simulations at hydrostatic scales. This study provides the first evidence supporting the use of convection-permitting global variable-resolution simulations for studying and improving forecasting of extreme precipitation over East China, and motivates the need for a more systematic study of heavy precipitation events and impacts of physics parameterizations and topography in the future.

1. Introduction

Extreme precipitation receives great attention because of its potential for generating flood, landslide, and other hazardous conditions. East China, occupied by more than 70% of the total population of China, is one of the areas with the most frequent intense extreme precipitation around the world (Zhai et al., 2005; Li et al., 2016). The socioeconomic development in regions such as the Yangtze River Delta region (YRD) in East China is remarkably vulnerable to extreme precipitation, making accurate forecast of extreme precipitation of great importance. The spatiotemporal variations of extreme precipitation over East China and their possible causes and underlying mechanisms have been investigated in many previous studies using observations and models (e.g., Ding et al., 2008; Zhang H. et al., 2011; Li et al., 2013; Zhang Q. et al., 2015, 2017; Hui et al., 2015; Liu et al., 2015; Li et al., 2016; Lin and Wang, 2016; Zhao et al., 2016; Zheng et al., 2016). Zhang et al. (2017) established a relationship between the western North Pacific subtropical high (WNPSH) and precipitation over East China and explored the underlying processes. Liu et al. (2015) analyzed data from the meteorological stations in East China and found significant increases in heavy precipitation at both rural and urban stations during 1955-2011. This enhanced precipitation intensity in East China has been partly attributed to localized daytime precipitation events (Guo et al., 2017). Recently, a regional climate model was used to simulate the regional climate extremes of China and noted large sensitivity of the simulated summer heavy precipitation over East China to the choice of cumulus parameterizations (Hui et al., 2015).

Numerical modeling is an important tool for understanding the underlying mechanisms of extreme precipitation and predicting precipitation characteristics that contributes to environmental impacts. Although precipitation modeling has improved in the last decades, accurate prediction of extreme precipitation remains challenging because of the multiscale nonlinear interactions of processes that generate heavy rainfall (Fritsch et al., 2004; Zhang et al., 2011; Sukovich et al. 2014). Although not a panacea for weather and climate modeling (NRC, 2012), previous studies suggested that increasing grid resolution could significantly improve modeling of extreme precipitation because the impacts of topography, land-use, land-atmosphere interaction, and other important processes are better resolved (e.g., Giorgi and Mearns, 1991; Giorgi and Marinucci, 1996; Leung et al., 2003; Bacmeister et al. 2014; ECMWF2016). With advances in computing and numerical modeling, convection-permitting modeling offers even more hope for reducing biases in simulating precipitation as convection and the strong vertical motions that are key to generating extreme precipitation are more

explicitly resolved (Pedersen and Winther, 2005; Déqué et al., 2007; Gao et al., 2017; Yang et al. 2017; Prein et al., 2015, 2017). Previous studies suggested that convection-permitting modeling is needed for more accurate prediction of the timing, distribution, and intensity of extreme precipitation events over China (e.g., Zhang et al., 2013; Xu et al., 2015).

Most studies of convection-permitting simulations have adopted non-hydrostatic regional models developed for weather forecasting or regional climate modeling (Prein et al. 2015). Global models capable of simulating non-hydrostatic dynamics are not as common as regional models, but they offer some advantages including the ability to provide global forecasts or simulations while avoiding numerical issues associated with lateral boundary conditions that are major sources of uncertainty in regional modeling and also limit regional feedback to large-scale circulation (e.g., Giorgi and Mearns, 1999; Wang et al. 2004; Laprise et al., 2008; Leung 2013; Prein et al. 2015). Non-hydrostatic global-variable resolution models, in particular, are useful as they allow convection-permitting simulations to be performed using regional refinement that significantly reduces computational cost compared to global convection-permitting modeling. Although global hydrostatic variable-resolution climate models, such as the variable-resolution version of Community Earth System Model, have been used in various applications in the last few years (e.g., Rauscher et al., 2013; Zarzycki et al., 2014, 2015; Rhoades et al., 2016; Huang et al., 2016; Wu et al., 2017; Gettelman, et al., 2018; Wang et al., 2018; Burakowski et al., 2019), so far few studies used global non-hydrostatic variable-resolution models to investigate weather or climate simulations, particularly at convection-permitting scales (e.g., Prein et al., 2015). This study explores the use of a non-hydrostatic global variable resolution model, the Model for Prediction Across Scales (MPAS) for modeling an extreme precipitation event in East China.

MPAS is a new multiscale modeling approach developed to take advantage of advances in mesh generation by employing the spherical centroidal Voronoi tessellations (SCVTs) (Du et al. 1999; Ringler et al. 2008). The SCVTs in MPAS enable local mesh refinement through the mesh generation process where a specified scalar density function determines higher and lower resolution regions in the mesh (see, e.g., Ju et al. 2011). Meshes can be configured with multiple high-resolution regions, and high resolution in one region does not need to be balanced by coarser resolution elsewhere. The underlying theory of SCVTs is robust concerning mesh properties and mesh generation. The atmospheric solver in MPAS (Skamarock et al, 2012) integrates the non-hydrostatic equations, and as such it is suitable for both weather and climate simulation, i.e. for both nonhydrostatic and hydrostatic flow simulation. MPAS has been evaluated and used in previous studies for investigating the resolution impact on modeling

clouds and precipitation (O'Brien et al., 2013; Zhao et al., 2016), the structure of the inter-tropical convergence zone (ITCZ) (Landu et al., 2014), precipitation extremes (Yang et al., 2014), atmospheric river frequency (Hagos et al., 2015), the position and strength of the eddy-driven jet (Lu et al., 2015), global atmospheric predictability at convection-permitting scales (Judt, 2018), and regional climate modeling (Sakaguchi et al., 2015, 2016). Except for Zhao et al. (2016) and Judt (2018), the aforementioned studies used a hydrostatic version of MPAS applied at resolutions ranging from ~25 km to 200 km.

To date, few studies have examined the MPAS performance in modeling extreme precipitation event, particularly at grid scales of ~10 km or less. In this study, we examine the MPAS performance in simulating a heavy precipitation event over East China and investigate its sensitivity to horizontal resolution and physics parameterizations. A heavy precipitation event that occurred on June 25-27 of 2012 over the YRD of East China is selected as it is one of the ten heaviest precipitation events in 2012. This rainfall event was triggered by a typical southwest vortex in the middle and high troposphere and wind shear in the lower layer of Meiyu front over East China during the East Asian summer monsoon (e.g., Xiang et al., 2013; Yao et al., 2017), initiated around 1200 UTC of 25 June. Most (more than two third) of heavy precipitation events over East China were caused by the wind shear of Meiyu front in last decades (Yao et al., 2017). During this period, a heavy precipitating system propagated along the Yangtze River and produced as much as 244 mm of precipitation in 24 hours at some locations. The continuous precipitation led to 17 deaths and about RMB 3.68 billion in total damage, and affected more than 685 million people in the provinces of Central and East China. Simulations are performed using MPAS (v5.2) with different cumulus and microphysics schemes. We first compare simulations produced using a global mesh with uniform resolution and a global variable resolution mesh with a refined region that has the same resolution as that of the global uniform mesh. The goal is to demonstrate the fidelity of global variable resolution modeling relative to the more computationally expensive global high-resolution modeling approach in regions that share the same horizontal resolution. The impacts of resolutions at hydrostatic scales (with convective parameterizations) and non-hydrostatic scales (i.e., convection-permitting scales with convection processes largely resolved) are also examined. The MPAS simulations are evaluated against weather station observations from the National Meteorological Information Center of the China Meteorological Administration (CMA). In addition, the modeling results are also compared with the forecasts produced by the Global Forecast System (GFS) of the National Centers for Environmental Prediction (NCEP).

The rest of the paper is organized as follows. Section 2 describes briefly the MPAS model, the physics parameterizations, and the model configuration for this study, followed by a description of data for evaluation. The series of global uniform and variable resolution experiments are analyzed in section 3. The findings are then summarized in section 4.

2. Data and methodology

2.1 Model and experiments

2.1.1 MPAS-Atmosphere (MPAS-A) model

This study uses a fully compressible non-hydrostatic model (MPAS v5.2) developed for weather prediction and climate applications. The non-hydrostatic dynamical core of MPAS is described in Skamarock et al. (2012). MPAS uses C-grid staggering of the prognostic variables and centroidal Voronoi meshes to discretize the sphere. The unstructured spherical centroidal Voronoi tessellation (SCVT) generation algorithms can provide global quasi-uniform resolution meshes as well as variable-resolution meshes through the use of a single scalar density function, hence opening opportunities for regional downscaling and upscaling between mesoscales and non-hydrostatic scales to hydrostatic scales within a global framework. The vertical discretization uses the height-based hybrid terrain-following coordinate (Klemp, 2011), in which coordinate surfaces are progressively smoothed with height to remove the impact of small-scale terrain structures. The dynamical solver applies the split-explicit technique (Klemp et al., 2007) to integrate the flux-form compressible equations. The basic temporal discretization uses the third order Runge-Kutta scheme and explicit time-splitting technique (Wicker and Skamarock, 2002), similar to that used in the Weather Research and Forecasting (WRF) model (Skamarock et al., 2008). The scalar transport scheme used by MPAS on its Voronoi mesh is described in Skamarock and Gassmann (2011), and the monotonic option is used for all moist species. The extensive tests of MPAS using idealized and realistic cases verify that smooth transitions between the fine- and coarse-resolution regions of the mesh lead to no significant distortions of the atmospheric flow (e.g., Skamarock et al., 2012; Park et al., 2013).

In the current version (v5.2) of MPAS, there are a few physics schemes available. Three convective parameterizations can be used. The Kain-Fritsch (KF, Kain, 2004) and the new Tiedtke (NTD, Bechtold et al., 2004, 2008, 2014) schemes represent both deep and shallow convection using a mass flux approach with a convective available potential energy (CAPE) removal time scale (Kain, 2004). The third one, the GF scheme (Grell and Freitas, 2014), is

based on the Grell-Devenyi ensemble scheme (Grell and Devenyi, 2002) using the multi-closure, multi-parameter, ensemble method but with improvements to smooth the transition to cloud-resolving scales following Arakawa et al. (2011). This scale-awareness is critical for global variable resolution simulation across hydrostatic (e.g., tens of km) and non-hydrostatic scales (e.g., 4 km). Fowler et al. (2016) implemented the GF convective parameterization in MPAS and examined the impacts of horizontal resolution on the partitioning between convective-parameterized and grid-resolved precipitation using a variable-resolution mesh in which the horizontal resolution varies between hydrostatic scales (~50 km) in the coarsest region of the mesh to non-hydrostatic scales (~ 3 km) in the most refined region of the mesh. For cloud microphysics, the WSM6 (Hong and Lim, 2006) and Thompson (Thompson et al., 2008) schemes, both of which are bulk microphysical parameterizations, are selected and compared. Both schemes include six hydrometeor species: water vapor, cloud water, rain, cloud ice, snow, and graupel (Gettelman et al., 2019). The WSM6 scheme is a one-moment prognostic parameterization, while the Thompson scheme includes a two-moment prognostic parameterization for cloud ice and the single-moment parameterization for the other hydrometeor species. The two schemes apply the same formula of gamma distribution of hydrometeor species: $N(D) = N_0 D^{\mu} e^{-\lambda D}$, where D is the particle diameter, N_0 is the intercept parameter, μ is the shape factor, and λ is the slope parameter, although the parameter values or functions vary in the two schemes. The mass-size relationship in WSM6 and Thompson is also expressed in the same formula as $m(D) = aD^b$. The mean falling speed is calculated as $V(D) = cD^d(\frac{\rho_0}{\rho})^{0.5}$ in WSM6 and $V(D) = cD^d(\frac{\rho_0}{\rho})^{0.5} exp\ (-fD)$ in Thompson, respectively (Hong and Lim, 2006; Thompson et al., 2008). In the formula, the WSM6 scheme assumes a power-law fit between terminal velocity and particle size as Locatelli and Hobbs (1974), while the Thompson scheme incorporates an exponential decay parameter to allow for a decrease in falling speed with increasing size (Molthan et al., 2012). Two options are available for representing the planetary boundary layer processes, the Mellor-Yamada-Nakanishi-Niino (MYNN) scheme (Nakanishi and Niino, 2006 and 2009) and the YSU scheme (Hong et al., 2006; Hong 2010). The Noah scheme (Chen and Dudhia, 2001) and the RRTMG scheme (Mlawer et al., 1997; Iacono et al., 2000) were implemented, respectively, for the land surface and radiative transfer processes.

2.1.2 Numerical experiments

In this study, the height coordinate of MPAS is configured with 55 layers, and the model top is at 30 km. Multiple experiments are conducted with MPAS using quasi-uniform resolution meshes and variable resolution meshes. Two quasi-uniform resolution meshes and three variable resolution meshes are configured, similar to those shown in Figure 1a and b that are coarsened to display the structure of the individual mesh cells. The quasi-uniform mesh has essentially the same mesh spacing globally, while the variable resolution mesh has finer mesh spacing in the refined region with a transition zone between the fine and coarse resolution meshes. More details about the mesh generation can be found in Ringler et al. (2011). The two quasi-uniform meshes have grid spacing that approximately equals to 15 km (U15km) and 60 km (U60km). The three variable resolution meshes feature a circular refined high-resolution region centered over East China as shown in Figure 1c. Figure 1c shows the exact mesh size distribution of the 4-60km variable resolution mesh (V4km) that has a refined region with grid spacing of approximately 4 km, and the mesh spacing gradually increases through a transition zone to approximately 60 km for the rest of the globe. The other two variable resolution meshes (V16km and V30km) have a similar mesh structure as the V4km mesh but with a mesh spacing of 16 km and 30 km, respectively, over the refined region that gradually increases to 128 km and 120 km, respectively, elsewhere.

Experiments U15km and V16km are compared to examine the difference between global uniform and variable resolution simulations in capturing the precipitation in the refined region, in order to explore the potential of regional refinement for regional weather and climate simulation. It is noteworthy here that the U15km mesh comprises ~2.5 million cells and the V16km mesh only comprises ~0.11 million cells. The difference in the number of mesh cells leads to a difference in computational and storage demand. With the TH-2 supercomputer of National Supercomputer Center in Guangzhou (NSCC-GZ), it takes ~9000 CPU hours and ~240 CPU hours to finish a one-day simulation for U15km and V16km, respectively. In addition, with the standard MPASv5.2, the sizes of output data per one-day simulation for U15km and V16km are 0.5 T and 0.02 T, respectively. The same time step of 60 second is used for physics and dynamics for both U15km and V16km simulations. In order to investigate the potential impact from physics parameterizations, two available convective parameterizations (GF and NTD) are used for each experiment with the two meshes. Two cloud microphysics schemes (WSM6 and Thompson) are also tested, but the precipitation differences in the U15km and V16km experiments are small. Therefore, only the results using WSM6 with two different convective parameterizations are shown in this study for the two meshes (U15km.NTD, U15km.GF, V16km.NTD, and V16km.GF).

The U60km, V30km, V16km, and V4km experiments are conducted to quantify the impacts of horizontal resolution on simulating precipitation characteristics. The numbers of grid cells in the U60km, V30km, V16km, and V4km meshes are ~0.16 million, 0.10 million, ~0.11 million, and ~0.8 million, respectively. Difference in the number of cell and minimum cell size also leads to a difference in computational and storage demand. With the TH-2 supercomputer of NSCC-GZ, it takes ~200 CPU hours, ~150 CPU hours, ~240 CPU hours, and ~1800 CPU hours to finish a one-day simulation for U60km, V30km, V16km, and V4km meshes, respectively. In addition, with the standard MPASv5.2, the sizes of output data per one-day simulation for the four meshes are 0.03 T, 0.02 T, 0.02 T, and 0.15 T, respectively. The time steps used for physics and dynamics for the four meshes are 300 seconds, 120 seconds, 60 seconds, and 20 seconds, respectively.

As discussed above, GF is the only convective parameterization that has been tested with scale-aware capability for using across the hydrostatic (e.g., tens of km) and non-hydrostatic scales (e.g., 4 km). Therefore, in order to investigate the difference among the experiments with the four meshes (U60km, V30km, V16km, and V4km), they are all conducted with the GF convective parameterization. Since the cloud microphysics has significant impact on the V4km simulations (discussed latter), the experiments of V4km with both WSM6 (V4km.WSM6) and Thompson (V4km.Thompson) cloud microphysics schemes are analyzed in this study. When examining the difference between the global uniform and variable resolution simulations and investigating the impact of mesh spacing, the same physics schemes and parameter values are used in multiple experiments if not specified explicitly. All the numerical experiments discussed above are summarized in Table 1.

Due to the large computing cost and data storage of the experiments conducted, particularly for the U15km and V4km experiments, this study does not perform ensemble simulations. Instead, the bootstrapping statistical analysis is used to test the statistical significance of the difference among multiple experiments investigated in this study. The bootstrap method uses resampling technique to extract certain samples, called bootstrap samples, within the range of the original data. Statistical metrics, such as averages, variances, correlation coefficient, can be calculated for each bootstrap sample. For a given confidence level (e.g., 95%), bootstrap confidence intervals of specific statistical metric can be estimated (e.g., Efron, 1992; Efron and Tibshirani, 1994).

To simulate the heavy precipitation event that occurred during June 25-27 of 2012 over the YRD of East China, all the MPAS experiments were initialized at 0000 UTC of 23 June 2012 to allow appropriate spin-up time, and the modeling results for 25-27 June 2012 are

analyzed. The simulations were initialized using the analysis data at 1° horizontal resolution at 0000 UTC of 23 June 2012 from the Global Forecast System (GFS) of National Center for Environmental Prediction (NCEP), the same as that used by the GFS forecast for the period. This way, the MPAS simulation results can also be compared against the GFS forecast starting from the 0000 UTC of 23 June 2012.

2.2 Dataset

Several datasets are used to evaluate the MPAS simulations. The hourly precipitation dataset from CMA is used for evaluating the simulated precipitation characteristics. The distribution of stations over the study domain is shown as the color-filled circles in Figure 2. The hourly wind field dataset from the ECMWF Reanalysis (ERA5) ($0.28^{o}\times0.28^{o}$) (https://rda.ucar.edu/datasets/ds630.0/) is used as the reference for evaluating the simulated distributions of winds. Lastly, the global forecast products at 0.5° and 1° horizontal resolutions starting from UTC00 of 23 June 2012 are also used for comparison. The GFS forecast products are downloaded from https://www.ncdc.noaa.gov/data-access/model-data/model-datasets/global-forcast-system-gfs. Since the focus of this study is not to investigate the difference between MPAS and GFS or to evaluate the performance of GFS, details about the GFS are not discussed here but can be found on the website listed above.

3. Results

3.1 Simulations at quasi-uniform and variable resolutions

Figure 2 shows the spatial distributions of precipitation and wind at 850 hPa averaged during the event (June 25 00:00 to June 27 12:00 UTC Time) from the simulations with global uniform (15 km) and variable (16 km over East China) resolutions (U15km.NTD and V16km.NTD). The mean precipitation from the CMA stations and the winds from the ERA-interim reanalysis are also shown. The CMA observations show average precipitation rate exceeding 50 mm/day over central East China with a heavy rain belt extending from west to east along 31°N. The rain belt is associated with the wind shear near the surface that is typically accompanied with the Meiyu front during the East Asian summer monsoon. In general, both simulations capture the observed precipitation pattern. It is evident that the modeling results over the refined region are consistent between the uniform and variable resolution simulations. The spatial correlation coefficient between the two simulations over the refined region (entire region shown in Fig. 2) is 0.85. Besides precipitation, both simulations also capture the

distribution of winds from the reanalysis data. The wind fields between the two simulations are also consistent with a spatial correlation coefficient of 0.99.

As mentioned above, the precipitation during this event is concentrated in a west-east narrow belt. For a more quantitative comparison, Figure 3 shows the zonal averaged precipitation during the event over East China (denoted as the black box in Fig. 2) from observations and simulations. The CMA observations show an evident precipitation peak reaching ~40 mm/day around the latitude of 31°N. All four simulations with different resolutions and convective parameterizations capture well the zonal distribution of observed precipitation. The correlation coefficients are 0.9 and 0.89 for the U15km and V16km simulations with the GF scheme, respectively, and 0.89 and 0.86 for the same simulations but with the NTD scheme. This comparison further indicates that the simulations at global uniform and variable resolutions are consistent with each other, with only negligible impacts from different convective parameterizations. Although this consistency does not depend on the convective schemes, simulations with the GF parameterization produce larger peak precipitation than those with the NTD parameterization and are more consistent with observations for this event. The impact of cloud microphysics (WSM6 and Thompson) on the consistency in modeling total precipitation is also examined and is found to be negligible (Fig. S1 and S2 in the supporting materials), although there are some impacts on the simulated grid-resolved precipitation (Fig. S3 in the supporting material).

Figure 4 shows the meridional precipitation propagation over East China during the event. The CMA observations indicate that the rain belt propagates from 26°N at 06 UTC of 25 June to 31°N at 00 UTC of 26 June and includes two precipitation peaks around 31°N. The rainfall reaches the first peak around 00 UTC of 26 June. The rain belt stays around 31°N and reaches the second peak around 00 UTC of 27 June. The event ends around 12 UTC of 27 June. The first precipitation peak was generated by the southwest-northeast wind shear line formed over Central East China along with a vortex over the Southwest at 00 UTC of 26 June. The shear line gradually extended eastward, leading to the second precipitation peak around 00 UTC of 27 June (Fig. S4 in the supporting material). All four experiments generally simulate the southwest vortex and wind shear during the event, although the strength and location do not match perfectly with the reanalysis. As the large-scale environment is quite well represented in the model, the simulations also generally capture the two peaks of precipitation along 31°N as observed. However, both U15km and V16km simulate a broader rain belt, resulting in positive biases of precipitation south of 30°N (Fig. S5 in the supporting materials).

Both simulations shift the first peak precipitation southward. In addition, the simulations extend the first peak precipitation period and shorten the second one to some extent (Fig. S5 in the supporting materials). The lower averaged total precipitation around 31°N from the simulation with the NTD parameterization (Fig. 3) is mainly due to the lower rainfall before 26 June compared to the one with the GF parameterization (Fig. S5). For the two precipitation peaks, the simulation with NTD is comparable to the one with GF. Although the two convective parameterizations lead to significant difference in simulating total precipitation before 26 June, both simulations generate consistent wind circulations at 700 hPa before 26 June with spatial correlation coefficients above 0.9 (over the domain as shown in Fig. S4 in the supporting material). Although the two convective parameterizations lead to different total precipitation, they have negligible impact on the consistency in modeling precipitation propagation using uniform and variable resolutions during this event. The correlation coefficients are 0.48 and 0.42 for the simulations with the GF scheme at the resolutions of U15km and V16km, respectively, and 0.55 and 0.54 for the simulations with the NTD scheme at the two resolutions. The results again indicate the consistency between the simulations at the global uniform and variable resolutions at hydrostatic scale over the refined region regardless of the convective parameterization used.

Overall, for the selected event, the MPAS simulations at global uniform and variable resolutions produce consistent results over the refined region with comparable horizontal resolution in terms of the spatial patterns of precipitation and wind fields and the precipitation propagation. This finding is in general agreement with the findings by previous studies of MPAS with idealized experiments (e.g., Zhao et al., 2016) and real-world experiments (e.g., Sakaguchi et al., 2015). These findings provide the basis for using global variable resolution configurations of MPAS for modeling extreme precipitation over East China. In the following, the impacts of resolution on modeling extreme precipitation during this event are investigated with multiple global variable-resolution experiments.

3.2 Impacts of resolution

3.2.1 Parameterized and resolved precipitation

Multiple experiments using MPAS at various resolutions are conducted as stated in the methodology section. The resolution crosses the scales from 60 km, 30 km, 16 km to 4 km. For global variable resolution configurations, a scale-aware convective parameterization is needed, especially for the configuration that crosses the hydrostatic (convective parameterization is

required) and non-hydrostatic scales (convection-permitting). Therefore, the experiments analyzed below are all conducted with the GF scheme that is developed for simulations down to ~ 4 km resolution (details can be found in Grell and Freitas, 2014). To demonstrate the scale-aware performance of the GF convective parameterization across various resolutions, Figure 5 shows the spatial distributions of convective parameterized and resolved precipitation averaged during the event. At the resolution of 60 km and 16 km, precipitation produced from the convective parameterization dominates the total precipitation amount. On the contrary, at the resolution of 4 km, the total precipitation amount from simulations with two different microphysics is dominated by the resolved precipitation. The fraction of parameterized precipitation in the total decreases significantly from the simulations at 16 km to the ones at 4km over the heavy precipitation region (Fig. S6 in the supporting materials). It is also interesting that the fraction of parameterized precipitation increases from the simulations at 60 km to the ones at 16 km to some extent. This demonstrates that the GF scheme is aware of the resolution change so the precipitation from the simulations at convection-permitting scale is mostly produced by the cloud microphysics in MPAS.

3.2.2 Spatial and temporal variation

Figure 6 shows the observed and simulated spatial distributions of precipitation and wind fields at 850 hPa averaged during the event. For comparison, the GFS forecast results at the resolutions of 1.0 degree and 0.5 degree are also included. The GFS forecast results from the two resolutions are similar, both showing a northward shifted rain belt compared to the CMA observation. Due to the northern shift of the rain belt, the spatial correlation coefficients between the GFS and the CMA observations over the entire region of Fig. 6 are only 0.06 and 0.03 for the resolutions of 1.0 degree and 0.5 degree, respectively. In comparison, the spatial correlation coefficients between the CMA observations and the MPAS simulations at the resolutions of 60 km, 30 km, and 16 km are 0.49, 0.47, and 0.56, respectively. The correlation coefficients for the 4 km simulations with the WSM6 and Thompson microphysics schemes are 0.63 and 0.54, respectively. In general, the experiments at the convection-permitting scale (4 km) capture better the observed precipitation pattern than simulations with convective parameterization over the refined region, although the performance is affected by the microphysics scheme to some extent.

In order to test the statistical significance of the difference among the experiments, the 95% confidence intervals of spatial correlation are estimated based on the bootstrap analysis. Although the correlation coefficients estimated above have an uncertain range, at the 95% confidence level the results still indicate that the V16km simulation produces better spatial

pattern of precipitation than other hydrostatic-scale simulations. In addition, the simulation at the convection-permitting scale is comparable to, if not better than, the V16km simulation. The results are summarized in Table 2. It is noteworthy that, although the difference in precipitation over East China is significant among the GFS forecasts at 0.5° and 1.0° resolutions and MPAS at various resolutions, their global distributions of precipitation and wind averaged during the event period are similar with spatial correlation coefficients of 0.40-0.43 (precipitation) and 0.86-0.93 (wind), respectively, against the satellite retrieved precipitation and ERA5 reanalysis wind (Fig. S7 in the supporting material).

The zonal distributions of precipitation can better demonstrate the difference among the simulations. Figure 7 shows the observed and simulated zonal distributions of precipitation averaged during the event over East China. For comparison, the GFS forecasts at 1°and 0.5° resolutions are also included. The modeling results are sampled at the CMA stations. Consistent with the spatial distributions of precipitation shown in Fig. 6, the GFS forecasts at both 0.5° and 1.0° resolutions reproduce the precipitation peak of ~40 mm/day but shift the rain belt northward by about 4.0° latitude from 31°N to 35°N. The MPAS simulations at 16 km and 30 km with the GF scheme can well capture the peak precipitation around 31°N, although the simulation at 30 km produces a second lower peak of precipitation around 29°N. The simulation at 60 km produces much lower precipitation peak of ~25 mm/day and shifts the rain belt southward to around 30°N. The underestimate of the simulation at 60 km is mainly due to the underestimate of the convective parameterized rain (Fig. 5). For the two MPAS simulations at 4 km, the precipitation is mainly generated by cloud microphysics (Fig. 5) and therefore can be significantly affected by the cloud microphysics schemes. The MPAS simulations at 4 km with WSM6 and Thompson produce different zonal distributions of the rain belt. The simulation using WSM6 reproduces the peak of precipitation, while the simulation using Thompson produces higher precipitation with a peak at 50 mm/day and shifts the peak northward by about 1 degree. Overall, the correlation coefficients between the CMA observations and the GFS forecasts are -0.19 and -0.15 for 0.5° and 1.0°, respectively, and the correlation coefficients are 0.68, 0.71, 0.89, and 0.97 (0.72) for the MPAS simulations at 60 km, 30 km, 16 km, and 4 km with the WSM6 (Thompson) cloud microphysics. At the 95% confidence level, the difference among the experiments is significant (Table 2).

Figure 8 compares the observed and simulated precipitation propagation during the event over East China. The modeling results are sampled at the CMA stations. The GFS forecasts at 0.5° and 1.0° are similar, and both generate a heavy precipitation zone between

34°N and 35°N that lasts for about 18 hours from UTC12 of June 26. This is largely different from the CMA observations, so the correlation coefficients between the forecasts and observations are only 0.02 and 0.03 for 0.5° and 1.0°, respectively. The northward shift of rain belt during the event (shown in Fig. 6 and 7) is related to the GFS forecast that only produced the second peak of precipitation around UTC 0000 of 27 June while totally missing the first peak. In addition, the GFS forecast overestimates the second peak and shift it towards the north by about 4°. The timing and location shift of the rain belt in the GFS forecast are mainly because of the bias of GFS in simulating the wind shear in this event. The GFS forecast failed to produce the southwest-northeast wind shear line around UTC 0000 of 26 June and generated too broad vortex over the west. Around UTC 0000 of 27 June, GFS simulated the wind shear line but locating it further north (Fig. S8 in the supporting material).

The MPAS simulations are highly dependent on the resolutions. All simulations roughly produce the two peaks of precipitation as observed during the event. However, the experiment at 60 km simulates the first precipitation peak southward and the second peak northward of the observations, while the experiment at 30 km simulates the second peak further south and a few hours earlier. The time and location shift corresponding well to biases in simulated wind shear (Fig. S8). The spatial correlation coefficients of precipitation are 0.30 and 0.32 between the observations and the simulations at 60 km and 30 km, respectively. The experiments at 16 km and 4 km with the WSM6 cloud microphysics scheme can better capture the timing and latitude of the observed precipitation event than U60km and V30km (Fig. S9 in the supporting materials), however both V16km and V4km overestimate the first peak precipitation and underestimate the second peak. The experiment at 4 km with the Thompson scheme overestimates the precipitation amount of both peaks. The correlation coefficients are 0.41 and 0.42 (0.38) for 16 km and 4 km with the WSM6 (Thompson) cloud microphysics schemes, respectively. At the 95% confidence level (Table 2), the experiments at 16 km and 4 km are comparable in terms of simulating the propagation of this rain belt and better than the experiments at other resolutions. It is interesting to note that MPAS and GFS forecasts, sharing the same initial condition, simulate different large-scale circulation particularly the wind shear structure with the system evolving (Fig. S8). The model capability in successfully capturing the wind shear structure during this event determines the performance in generating the rain belt evolution. The formation and evolution of wind shear during the Meiyu front over East China have been found interacting with multiscale processes and systems, including terrain and convective latent heat (Yao et al., 2017). Different representation of the terrain over East China

in various resolutions may impact the simulated wind shear structure. Previous studies also found that convective latent heat may vary with resolutions and physics (Hagos et al., 2013; Zhao et al., 2016), which can further affect the simulation of wind shear structure. Therefore, the difference in resolution and physics between MPAS and GFS may result in their difference in simulating the formation and evolution of wind shear structure during the event. A more detailed exploration of the differences between the MPAS and GFS simulations is beyond the scope of this study.

The spatial distribution of the rain belt can also be reflected by the vertical wind distributions. Figure 9 compares the height-latitude cross section of the winds averaged over the region (shown as in Fig. 6) during the event from the ERA5 reanalysis, the GFS forecasts, and the MPAS simulations. In the ERA5 reanalysis wind fields, vertical motion is located primarily around 31°N, extending from the lower troposphere (~900 hPa) to the upper troposphere (~200 hPa). The GFS simulates the vertical motion primarily around 33°N, but the vertical motion is also strong around 35°N from 600 hPa to 200 hPa, which can be linked to the heavy precipitation generated there. These biases result in weaker correlation in vertical winds between the reanalysis and the GFS forecasts with coefficients of 0.29 and 0.32 for 0.5° and 1.0° resolutions, respectively. The MPAS experiment at 60 km simulates the vertical motion toward the south around 28°N. The MPAS experiments at 30 km and 16 km generally agree well with the ERA5 reanalysis, although both generate higher vertical motion in the south (e.g. 25°N) to some extent. The correlation coefficients between the reanalysis and the MPAS experiments at 60 km, 30 km, and 16 km are 0.53, 0.68, and 0.80, respectively. The MPAS experiment at 4 km with the WSM6 scheme produces consistent vertical motion with that in the ERA5 reanalysis, while the one with the Thompson scheme shifts the vertical motion a little further north. Both experiments at 4 km have the highest correlation in the distributions of vertical motion with the reanalysis with coefficients of 0.85 and 0.80 for WSM6 and Thompson, respectively. The statistical significance tests based on the bootstrap analysis indicate that at the 95% confidence level the model performance at 16 km and 4 km in terms of simulating vertical structure of winds are comparable and better than the simulations at coarser resolution (Table 2). The zonal distributions of precipitation discussed above correspond well with the distributions of vertical motion in all the experiments. Differences in the spatial distribution of vertical motions suggest that model resolution, and in some degree cloud microphysics parameterizations, have important effects on simulating the structure of the

wind shear over East China during the East Asian summer monsoon and the embedded precipitation.

3.2.3 Distribution of extreme precipitation

Besides predicting the spatial and temporal variations of the rain belt, it is also critical to capture the location and intensity of extreme precipitation within the heavy rain belt. Since the GFS forecasts shift the entire rain belt northward, only the MPAS simulations are analyzed here. Figure 10 shows the spatial distributions of precipitation averaged during the event over the heavy rain region (27°N-32°N and 110°E-122°E). The CMA observations show that heavy precipitation exceeding 50 mm/day mainly occurs over the plains of South Anhui province and Southeast Hubei province and part of the Huang Mountains. The MPAS experiment at 60 km simulates much smaller areas with heavy precipitation exceeding 50 mm/day. In addition, it simulates heavy precipitation over some areas of Hunan province, which is not observed by the CMA stations. The experiment at 30 km produces more numerous areas with heavy precipitation and captures the locations of heavy precipitation over the Huang Mountains. However, it misses the heavy precipitation over the plains of South Anhui province and Southeast Hubei province; instead, it produces heavy precipitation over large areas of mountainous regions over Hunan and Jiangxi provinces. The experiment at 16 km simulates better spatial distribution of heavy precipitation, particularly capturing the heavy precipitation over the Huang Mountains and the plain of South Anhui province, although it still shifts the heavy precipitation from Southeast Hubei province to Hunan province. The experiments at 4 km are affected by the cloud microphysics. The 4 km experiment with the WSM6 scheme produces the best spatial distribution among the MPAS experiments. It generally captures the observed heavy precipitation areas during this event as discussed above, although the locations do not perfectly match that of the observations. On the other hand, the 4 km experiment with the Thompson microphysics produces more areas of heavy precipitation over Central Anhui province. As a result, the correlation coefficients between the observations and the MPAS experiments at the resolutions of 60 km, 30 km, 16 km, and 4 km are 0.20, 0.21, 0.29, 0.50 (WSM6), and 0.42 (Thompson), respectively. The statistical significance test based on the bootstrap analysis indicates that at the 95% confidence level the simulations at 4 km can better capture the spatial distribution of heavy precipitation than the simulations at resolutions of hydrostatic scale (Table 2).

Figure 11 shows the probability density functions (PDFs) of hourly precipitation at all the CMA stations during the event. Precipitation above ~5 mm/hour (~120 mm/day) is considered very heavy and extra heavy storm rain event (refer to the CMA definition) that may cause dramatic flooding and damage locally or regionally. During this event, for precipitation lower than ~5 mm/hour, the MPAS simulations at hydrostatic scales (60 km, 30 km, and 16 km) overestimate the frequency, while above ~5 mm/hour, these simulations significantly underestimate the frequency. In contrast, the MPAS simulations at convection-permitting scale (4 km) produce much higher frequency of extreme precipitation above ~5 mm/hour, more consistent with the observations. However, the simulated frequency of extreme precipitation at convection-permitting scale depends on the cloud microphysics schemes. The Thompson scheme produces much higher frequency than the WSM6 scheme and results in a positive bias relative to the observations during this event, which deserves further investigation in future. The results also indicate that the convective parameterization appears not to be able to produce the higher intensity precipitation.

Previous studies found that the distribution of extreme precipitation correlates well with that of the lower tropospheric upward vertical velocity (e.g., Zhao et al., 2016). Figure 12 shows the PDFs of hourly upward vertical velocity averaged below 700 hPa at all the CMA stations during the event from the MPAS simulations. In general, the comparison of lower-level upward vertical velocity among the experiments is consistent with that of precipitation (Fig. 11) in that simulations at hydrostatic scales (i.e., 60 km, 30 km, and 16 km in this study) produce higher frequencies of updrafts < 4 cm/s than simulations at 4 km and vice versa for stronger updrafts. The difference in updrafts between the 4 km MPAS simulations with two different cloud microphysics schemes is negligible. Another analysis with the simulated updrafts at various resolutions all regridded to 0.5° resolution shows the similar PDFs as Fig. 12. Previous studies have proposed some mechanisms underlying the resolution impacts on modeling vertical velocity (e.g., Rauscher et al., 2016; Jeevanjee et al., 2017; Herrington and Reed, 2017; O'Brien et al., 2016; Fildier et al., 2018). Among these mechanisms, Rauscher et al. (2016) argued that the resolution-dependent vertical velocity is caused by the interaction between the constraint of fluid continuity and macro-scale turbulence. They suggested that the vertical velocity should be more intense at higher resolution because the horizontal velocity increment follows approximately a power law of resolution. Therefore, the resolved vertical transport must increase as grid spacing decreases. Assuming atmospheric moisture is relatively

588 insensitive to resolution, the upward moisture flux should increase as grid spacing decreases,
589 hence producing more precipitation.
590 Figure 13 shows the PDFs of the upward moisture flux and the relationship between
591 hourly precipitation versus upward moisture flux at 850hPa during the event from the MPAS
592 simulations at 60km, 30km, 16km and 4km. It is evident that the simulations at higher
593 resolutions produce more frequent intense upward moisture fluxes at 850hPa, consistent with
594 Rauscher et al. (2016) and O'Brien et al. (2016). Rauscher et al. (2016) found a linear
595 relationship between precipitation and upward moisture fluxes at lower level. The relationship
596 lines from this study as shown in Fig. 13 parallel the 1:1 reference line for all resolutions.
597 However, the lines are consistently below the reference line for the convection-permitting
598 simulations (4km) and are above the reference line for the hydrostatic simulations with
599 convective parameterization (e.g., 16km, 30km, 60km). The simulated precipitation can be
600 larger than the lower level upward moisture fluxes at hydrostatic scale because part of the
601 precipitation is contributed by the convective parameterization rather than contributed by the
602 resolved upward moisture flux (Rauscher et al., 2016). On the contrary, precipitation could be
603 lower than the upward moisture flux at convection-permitting scale (e.g., 4km) as moisture is
604 removed from cloud updrafts due to detrainment (e.g., O'Brien et al., 2016). Overall, our results
605 of the resolution-dependent updraft and precipitation are consistent with Rauscher et al. (2016)
606 and O'Brien et al. (2016).
607

608 ## 4. Summary and discussion

609 In this study, a series of MPAS simulations of a heavy precipitation event over East
610 China, triggered by a typical southwest vortex in the middle and high troposphere and wind
611 shear in the lower layer of the Meiyu front during the East Asian summer monsoon, are
612 compared. The simulations are performed at various resolutions from hydrostatic (60 km, 30
613 km, 16 km) to non-hydrostatic (4 km) scales. Consistency between the MPAS simulations at
614 global uniform and variable resolutions is also investigated. Besides the impacts of resolution
615 on simulating heavy precipitation, the impacts of convective and cloud microphysics schemes
616 are also examined. All the MPAS simulations are evaluated using the CMA station
617 observations of precipitation and the ERA5 reanalysis of winds, and compared against the
618 NCEP GFS forecasts that share the same initial condition of the MPAS simulations.
619 In general, the MPAS simulations at global uniform (U15km) and variable (V16km)
620 resolutions produce similar results in terms of the spatial and temporal distributions of

precipitation and winds inside the refined region over East China. Both experiments can capture the observed precipitation characteristics. This suggests that the global variable-resolution configuration of MPAS may be appropriate to simulate heavy precipitation over East China, which is also consistent with the finding from previous studies using variable resolution MPAS with regional refinement over other parts of the globe (e.g., Sakaguchi et al., 2015; Zhao et al., 2016). The simulations with two different convective parameterizations show that the MPAS simulated distributions of precipitation are affected by the convective schemes at hydrostatic scales, while the impacts from the cloud microphysics schemes are small.

Further investigation of MPAS experiments at multiple resolutions from hydrostatic (60 km, 30 km, 16 km) to non-hydrostatic (4 km) scales over East China shows significant impacts of resolution on simulating the spatial distributions of precipitation and winds. The variable-resolution simulations spanning hydrostatic and non-hydrostatic scales reveal that the scale-aware GF convective parameterization produces less convective parameterized precipitation as the horizontal resolution increases. Meanwhile, the subgrid-scale motions become increasingly resolved and the ratio of grid-scale to total precipitation increases over the refined region as resolution increases to 4 km. Comparison against the station observations indicates that the MPAS simulations at 16 km and 4 km can generally better capture the observed temporal and zonal distribution of the rain belt in the simulated event than the simulations at coarser resolutions. The simulations at coarser resolutions of 60 km and 30 km produce weaker precipitation and a southward shift of the rain belt. In contrast, the GFS forecasts at 0.5° and 1.0° produce a northward shift of the rain belt. The analysis also indicates the significant impacts from cloud microphysics on the MPAS simulations at 4 km in terms of precipitation distribution and intensity. The biases in the locations of rain belt are mainly due to failure of the model to simulate the wind shear structure of the Meiyu front during this event. The distributions of rain belt are consistent with the zonal shift of vertical motion. This suggests that the position and structure of the wind shear of the Meiyu front that produces the vertical motion is sensitive to the models and their specific configurations even though all simulations share the same initial condition. Previous studies have found that the formation and evolution of wind shear during the Meiyu front can interact with multiscale processes and systems over East China, including terrain and convective latent heat (Yao et al., 2017). Therefore, different representation of the terrain over East China in various resolutions and convective latent heat resulted from different physics schemes may affect the simulated wind shear structure among the MPAS experiments at various resolutions and between MPAS and GFS.

Besides the general zonal distribution of the rain belt, the distribution and intensity of heavy precipitation are also investigated. The experiments at 4 km can better capture the areas with heavy precipitation (> 50 mm/day) than the experiments at coarser resolutions compared to the observations, although the simulations at 4 km overestimate the first peak precipitation and underestimate the second one. In addition, the MPAS simulations at 4 km can better generate the frequency of intense precipitation that is significantly underestimated by simulations at coarser resolutions, which may indicate that the convective parameterization appears not to be able to produce intense precipitation. The analysis also shows that the underestimation of intense precipitation is consistent with the underestimation of resolved upward motions in the simulations at coarser resolutions. Although the MPAS simulations at 4 km generally produce better results than the experiments at coarser resolutions particularly 30 km and up, they still have some biases in the timing and intensity of precipitation. In addition, the performance of MPAS at convection-permitting scale is quite sensitive to the cloud microphysics scheme in terms of the distribution and intensity of extreme precipitation. This is consistent with Feng et al. (2018), who found that cloud microphysics parameterizations in convection permitting regional simulations have important effects on macroscale properties such as the lifetime, precipitation amount, stratiform versus convective rain volumes of mesoscale convective systems in the U.S. They attributed the impacts to the representation of ice phase hydrometeor species that influence the mesoscale convective systems through their influence on the diabatic heating profiles that provide dynamical feedback to the circulation (Yang et al. 2017). Hence more efforts may be needed to improve cloud microphysics processes for modeling extreme precipitation at convection-permitting scale in the future. In the meantime, aerosols have been found to play a critical role in simulating some heavy precipitation events over China through their impacts on cloud microphysics and/or radiation (e.g., Zhong et al., 2015, 2017; Fan et al., 2015). The current version of MPAS does not represent aerosol-radiation and aerosol-cloud interactions, which may also contribute to the biases of extreme precipitation at convection-permitting scales. Lastly, it is also noteworthy that the resolution of 4 km may still be insufficient to resolve some convective cells, which may also contribute to the modeling biases (Bryan and Morrison, 2012).

This study provides the first evidence supporting the use of global variable resolution configuration of MPAS for simulating extreme precipitation events over East China. In particular, the MPAS variable-resolution experiment at convection-permitting scale (4 km) improves the simulated distribution and intensity of precipitation over the area of interest, which is consistent with previous studies using regional convection permitting models (e.g.,

Zhang et al., 2013; Prein et al., 2015; Yang et al. 2017; Gao et al. 2017; Feng et al. 2018). The higher resolution MPAS experiments simulate better spatial distribution of heavy precipitation over the complex topographic region of East China, which suggests that topography may play a critical role and deserves further investigation in the future. Our results show that cloud microphysics parameterizations have important effects in convection permitting simulations, but modeling of other physical processes such as boundary layer turbulence, radiation, and aerosols may also affect the skill of convection permitting simulations. The GFS forecasts analyzed in this study show significant biases in precipitation distribution. The zonal shift of the rain belt by the MPAS simulations at coarser resolutions compared to simulations at finer resolutions suggests that resolution may have contributed to the GFS forecast biases. A more detailed exploration of the differences between the MPAS and GFS simulations is beyond the scope of this study.

Previous studies (Xue et al., 2007; Clark et al. 2016) noted the importance of ensemble simulations in predicting heavy precipitation. Due to the computational limitation, only one set of experiments with different physics and resolutions are evaluated in this study. The MPAS simulations of heavy precipitation with different initial conditions and refinement sizes deserve more evaluations. Finally, some studies noted that convection-permitting modeling does not always add values in simulating heavy precipitation compared to hydrostatic scale modeling (e.g., Kain et al., 2008; Rhoades et al., 2018; Xu et al., 2018). Rhoades et al. (2018) found that the improvement by increasing resolution may also depend on cloud microphysics parameterization. Increasing horizontal resolution alone sometimes can even lead to worse model performance. The impacts of increasing horizontal resolution on the overall model performance in simulating extreme precipitation may also be affected by the model structure and coupling among model components and processes (Jeevanjee et al., 2016; O'Brien et al., 2016; Herrington et al., 2017, 2018; Gross et al., 2018). This study also found some sensitivity of modeling extreme precipitation to cloud microphysics, particularly at convection-permitting scale. More events of heavy precipitation over East China should be investigated in the future to more systematically evaluate the MPAS variable-resolution modeling framework and the impacts of resolution and physical parameterizations.

Code availability

The MPAS release v5.2 can be obtained at *mpas-dev.github.io*. Global meshes generated for the experiments used in this study are available upon request by contacting the corresponding author.

722

723 **Author contributions**

724 CZ and YW designed research. MX performed the simulations. CZ, MX, MZ, and ZH analyzed
725 the simulations. JG collected and analyzed the observations. CZ, MX, and YW wrote the paper.
726 LRL, MD, and WS guided the experiment design and edited the paper.

727

728 ## Acknowledgements

729 This research was supported by the Ministry of Science and Technology of China under grant
730 2017YFC1501401 and the Fundamental Research Funds for the Central Universities. The
731 study used computing resources from the High-Performance Computing Center of University
732 of Science and Technology of China (USTC) and the TH-2 of National Supercomputer Center
733 in Guangzhou (NSCC-GZ). Leung was supported by the U.S. Department of Energy Office of
734 Science Biological and Environmental Research as part of the Regional and Global Modeling
735 and Analysis program. PNNL is operated for the Department of Energy under contract DE-
736 AC05-76RL01830.

737

Reference

Arakawa, A., Jung, J. H., & Wu, C. M.: Toward unification of the multiscale modeling of the atmosphere. Atmospheric Chemistry and Physics, 11(8), 3731-3742. https://doi.org/10.5194/acp-11-3731-2011, 2011.

Bacmeister, J. T., Wehner, M. F., Neale, R. B., Gettelman, A., Hannay, C., Lauritzen, P. H., ... & Truesdale, J. E.: Exploratory high-resolution climate simulations using the Community Atmosphere Model (CAM). Journal of Climate, 27(9), 3073-3099. https://doi.org/10.1175/JCLI-D-13-00387.1, 2014.

Bechtold, P., Chaboureau, J. P., Beljaars, A., Betts, A. K., Köhler, M., Miller, M., & Redelsperger, J. L.: The simulation of the diurnal cycle of convective precipitation over land in a global model. Quarterly Journal of the Royal Meteorological Society, 130(604), 3119-3137. https://doi.org/10.1256/qj.03.103, 2004.

Bechtold, P., Köhler, M., Jung, T., Doblas-Reyes, F., Leutbecher, M., Rodwell, M. J., ... & Balsamo, G.: Advances in simulating atmospheric variability with the ECMWF model: From synoptic to decadal time-scales. Quarterly Journal of the Royal Meteorological Society, 134(634), 1337-1351. https://doi.org/10.1002/qj.289, 2008.

Bechtold, P., Semane, N., Lopez, P., Chaboureau, J. P., Beljaars, A., & Bormann, N.: Representing equilibrium and nonequilibrium convection in large-scale models. Journal of the Atmospheric Sciences, 71(2), 734-753. https://doi.org/10.1175/JAS-D-13-0163.1, 2014.

Bryan, G. H., and H. Morrison: Sensitivity of a simulated squall line to horizontal resolution and parameterization of microphysics. Mon. Wea. Rev., 140, 202–225, https://doi.org/10.1175/MWR-D-11-00046.1, 2012.

Burakowski, E. A., Tawfik, A., Ouimette, A., Lepine, L., Zarzycki, C., Novick, K., ... & Bonan, G.: Simulating surface energy fluxes using the variable-resolution Community Earth System Model (VR-CESM). Theoretical and Applied Climatology, 1-19. https://doi.org/10.1007/s00704-019-02785-0, 2019.

Chauvin, F., J.-F. Royer, and M. Deque: Response of hurricane type vortices to global warming as simulated by ARPEGE-Climat at high resolution. Climate Dyn., 27, 377-399, https://doi.org/10.1007/s00382-006-0135-7, 2006.

Chen, F., & Dudhia, J.: Coupling an advanced land surface–hydrology model with the Penn State–NCAR MM5 modeling system. Part I: Model implementation and

sensitivity. Monthly Weather Review, 129(4), 569-585. https://doi.org/10.1175/1520-0493(2001)129<0569:CAALSH>2.0.CO;2, 2001.

Déqué, M., Jones, R. G., Wild, M., Giorgi, F., Christensen, J. H., Hassell, D. C., ... & De Castro, M.: Global high resolution versus Limited Area Model climate change projections over Europe: quantifying confidence level from PRUDENCE results. Climate Dynamics, 25(6), 653-670. https://doi.org/10.1007/s00382-005-0052-1, 2005.

Déqué, M., & Piedelievre, J. P.: High resolution climate simulation over Europe. Climate dynamics, 11(6), 321-339. https://doi.org/10.1007/BF00215735, 1995.

Déqué, M., Rowell, D. P., Lüthi, D., Giorgi, F., Christensen, J. H., Rockel, B., ... & van den Hurk, B. J. J. M.: An intercomparison of regional climate simulations for Europe: assessing uncertainties in model projections. Climatic Change, 81(1), 53-70. https://doi.org/10.1007/s10584-006-9228-x, 2007.

Ding, Y., Wang, Z., & Sun, Y.: Inter-decadal variation of the summer precipitation in East China and its association with decreasing Asian summer monsoon. Part I: Observed evidences. International Journal of Climatology, 28(9), 1139-1161. https://doi.org/10.1002/joc.1615, 2008.

Clark, P., Roberts, N., Lean, H., Ballard, S. P., & Charlton-Perez, C.: Convection-permitting models: a step-change in rainfall forecasting. Meteorological Applications, 23(2), 165-181. https://doi.org/10.1002/met.1538, 2016.

Du, Q., Faber, V., & Gunzburger, M.: Centroidal Voronoi tessellations: Applications and algorithms. SIAM review, 41(4), 637-676. https://doi.org/10.1137/S0036144599352836, 1999.

ECMWF: ECMWF strategy 2016–2025: The strength of a common goal. European Centre for Medium-Range Weather Forecasts Tech. Rep., 32 pp.https://www.ecmwf.int/sites/default/files/ECMWF_Strategy_2016-2025.pdf, 2016.

Efron, B.: Bootstrap methods: another look at the jackknife. In Breakthroughs in statistics (pp. 569-593). Springer, New York, NY. https://doi.org/10.1007/978-1-4612-4380-9_41, 1992.

Efron, B., & Tibshirani, R. J.: An introduction to the bootstrap. CRC press, 1994.

Fan, J., Rosenfeld, D., Yang, Y., Zhao, C., Leung, L. R., & Li, Z.: Substantial contribution of anthropogenic air pollution to catastrophic floods in Southwest China. Geophysical Research Letters, 42(14), 6066-6075. https://doi.org/10.1002/2015GL064479, 2015.

802 Feng, Z., L.R. Leung, R.A. Houze, Jr., S. Hagos, J. Hardin, Q. Yang. B. Han, & J. Fan:
803 Structure and evolution of mesoscale convective systems: sensitivity to cloud
804 microphysics in convection-permitting simulations over the U.S. J. Adv. Model. Earth
805 Syst., 10, https://doi.org/10.1029/2018MS001305, 2018.
806 Fowler, L. D., Skamarock, W. C., Grell, G. A., Freitas, S. R., & Duda, M. G.: Analyzing the
807 Grell–Freitas convection scheme from hydrostatic to nonhydrostatic scales within a
808 global model. Monthly Weather Review, 144(6), 2285-2306.
809 https://doi.org/10.1175/MWR-D-15-0311.1, 2016.
810 Fritsch, J. M., & Carbone, R. E.: Improving quantitative precipitation forecasts in the warm
811 season: A USWRP research and development strategy. Bulletin of the American
812 Meteorological Society, 85(7), 955-966. https://doi.org/10.1175/BAMS-85-7-955,
813 2004.
814 Gao, Y., L.R. Leung, C. Zhao, & S. Hagos: Sensitivity of summer precipitation to model
815 resolution and convective parameterizations across gray zone resolutions. J. Geophys.
816 Res., 122, 2714-2733, doi:10.1002/2016JD025896, 2017.
817 Gettelman, A., Callaghan, P., Larson, V. E., Zarzycki, C. M., Bacmeister, J. T., Lauritzen, P.
818 H., ... & Neale, R. B.: Regional climate simulations with the community earth system
819 model. Journal of Advances in Modeling Earth Systems, 10(6), 1245-1265.
820 https://doi.org/10.1002/2017MS001227, 2018.
821 Gettelman A., Morrison H., Thompson G.: Cloud Microphysics Across Scales for Weather and
822 Climate. In: Randall D., Srinivasan J., Nanjundiah R., Mukhopadhyay P. (eds) Current
823 Trends in the Representation of Physical Processes in Weather andClimate Models.
824 Springer Atmospheric Sciences. Springer, Singapore, 2019.
825 Giorgi, F., and Marinucci, M. R.: A investigation of the sensitivity of simulated precipitation
826 to model resolution and its implications for climate studies. Monthly Weather
827 Review, 124(1), 148-166. https://doi.org/10.1175/1520-
828 0493(1996)124<0148:AIOTSO>2.0.CO;2, 1996.
829 Giorgi, F., and Mearns, L. O.: Approaches to the simulation of regional climate change: a
830 review. Reviews of Geophysics, 29(2), 191-216. https://doi.org/10.1029/90RG02636,
831 1991.
832 Grell, G. A., & Dévényi, D.: A generalized approach to parameterizing convection combining
833 ensemble and data assimilation techniques. Geophysical Research Letters, 29(14), 38-
834 1. https://doi.org/10.1029/2002GL015311, 2002.

Grell, G. A., & Freitas, S. R.: A scale and aerosol aware stochastic convective parameterization for weather and air quality modeling. Atmos. Chem. Phys, 14(10), 5233-5250. https://doi.org/10.5194/acp-14-5233-2014, 2014.

Gross, M., Wan, H., Rasch, P. J., Caldwell, P. M., Williamson, D. L., Klocke, D., Christiane, J, Diana, T., Nigel, W., Mike, C, Bob, B., Martin, W., Florian, L., Eric, B., Sylvie, M., Piet, T., Almut, G., Peter, L., Hans, J., Colin, Z., Sakaguchi, K., Leung, R.: Physics–Dynamics Coupling in Weather, Climate, and Earth System Models: Challenges and Recent Progress. Monthly Weather Review, 146(11), 3505-3544. https://doi.org/10.1175/MWR-D-17-0345.1, 2018.

Guo, J., Su, T., Li, Z., Miao, Y., Li, J., Liu, H., Xu, H., Cribb, M., and Zhai, P.: Declining frequency of summertime local-scale precipitation over eastern China from 1970 to 2010 and its potential link to aerosols. Geophysical Research Letters, 44(11), 5700-5708, 2017.

Hagos, S., Leung, L. R., Yang, Q., Zhao, C., and Lu, J.: Resolution and dynamical core dependence of atmospheric river frequency in global model simulations. Journal of Climate, 28(7), 2764-2776. https://doi.org/10.1175/JCLI-D-14-00567.1, 2015.

Herrington, A. R., & Reed, K. A.: An explanation for the sensitivity of the mean state of the community atmosphere model to horizontal resolution on aquaplanets. Journal of Climate, 30(13), 4781-4797. https://doi.org/10.1175/JCLI-D-16-0069.1, 2017.

Herrington, A. R., & Reed, K. A.: An Idealized Test of the Response of the Community Atmosphere Model to Near - Grid - Scale Forcing Across Hydrostatic Resolutions. Journal of Advances in Modeling Earth Systems, 10(2), 560-575. https://doi.org/10.1002/2017MS001078, 2018.

Fildier, B., Parishani, H., & Collins, W. D.: Prognostic Power of Extreme Rainfall Scaling Formulas Across Space and Time Scales. Journal of Advances in Modeling Earth Systems, 10(12), 3252-3267. https://doi.org/10.1029/2018MS001462, 2018.

Hong, S. Y.: A new stable boundary-layer mixing scheme and its impact on the simulated East Asian summer monsoon. Quarterly Journal of the Royal Meteorological Society, 136(651), 1481-1496. https://doi.org/10.1002/qj.665, 2010.

Hong, S. Y., & Lim, J. O. J.: The WRF single-moment 6-class microphysics scheme (WSM6). J. Korean Meteor. Soc, 42(2), 129-151, 2006.

Hong, S. Y., Noh, Y., & Dudhia, J.: A new vertical diffusion package with an explicit treatment of entrainment processes. Monthly weather review, 134(9), 2318-2341. https://doi.org/10.1175/MWR3199.1, 2006.

Huang, X., Rhoades, A. M., Ullrich, P. A., & Zarzycki, C. M.: An evaluation of the variable-resolution CESM for modeling California's climate. Journal of Advances in Modeling Earth Systems, 8(1), 345-369. https://doi.org/10.1002/2015MS000559, 2016.

Hui, P., Tang, J., Wang, S., & Wu, J.: Sensitivity of simulated extreme precipitation and temperature to convective parameterization using RegCM3 in China. Theoretical and applied climatology, 122(1-2), 315-335. https://doi.org/10.1007/s00704-014-1300-2, 2015.

Iacono, M. J., Mlawer, E. J., Clough, S. A., & Morcrette, J. J.: Impact of an improved longwave radiation model, RRTM, on the energy budget and thermodynamic properties of the NCAR community climate model, CCM3. Journal of Geophysical Research: Atmospheres, 105(D11), 14873-14890. https://doi.org/10.1029/2000JD900091, 2000.

Jeevanjee, N.: Vertical velocity in the gray zone. Journal of Advances in Modeling Earth Systems, 9(6), 2304-2316. https://doi.org/10.1002/2017MS001059, 2017.

Judt, F.: Insights into Atmospheric Predictability through Global Convection-Permitting Model Simulations. Journal of the Atmospheric Sciences, 75(5), 1477-1497. https://doi.org/10.1175/JAS-D-17-0343.1, 2018.

Ju, L., Ringler, T., & Gunzburger, M.: Voronoi tessellations and their application to climate and global modeling. In Numerical techniques for global atmospheric models (pp. 313-342). Springer, Berlin, Heidelberg. https://doi.org/10.1007/978-3-642-11640-7_10, 2011.

Kain, J. S.: The Kain–Fritsch convective parameterization: an update. Journal of applied meteorology, 43(1), 170-181. https://doi.org/10.1175/1520-0450(2004)043<0170:TKCPAU>2.0.CO;2, 2004.

Kain, J. S., Weiss, S. J., Bright, D. R., Baldwin, M. E., Levit, J. J., Carbin, G. W., ... & Thomas, K. W.: Some practical considerations regarding horizontal resolution in the first generation of operational convection-allowing NWP. Weather and Forecasting, 23(5), 931-952. https://doi.org/10.1175/WAF2007106.1, 2008.

Klemp, J. B.: A terrain-following coordinate with smoothed coordinate surfaces. Monthly weather review, 139(7), 2163-2169. https://doi.org/10.1175/MWR-D-10-05046.1, 2011.

Klemp, J. B., Skamarock, W. C., & Dudhia, J.: Conservative split-explicit time integration methods for the compressible nonhydrostatic equations. Monthly Weather Review, 135(8), 2897-2913. https://doi.org/10.1175/MWR3440.1, 2007.

Landu, K., Leung, L. R., Hagos, S., Vinoj, V., Rauscher, S. A., Ringler, T., & Taylor, M.: The dependence of ITCZ structure on model resolution and dynamical core in aquaplanet simulations. Journal of Climate, 27(6), 2375-2385. https://doi.org/10.1175/JCLI-D-13-00269.1, 2014.

Laprise, R.: Regional climate modelling. Journal of Computational Physics, 227(7), 3641-3666. https://doi.org/10.1016/j.jcp.2006.10.024, 2008.

Leung, L. R., & Qian, Y.: The sensitivity of precipitation and snowpack simulations to model resolution via nesting in regions of complex terrain. Journal of Hydrometeorology, 4(6), 1025-1043. https://doi.org/10.1175/1525-7541(2003)004<1025:TSOPAS>2.0.CO;2, 2003.

Leung, L. R., Ringler, T., Collins, W. D., Taylor, M., & Ashfaq, M.: A hierarchical evaluation of regional climate simulations. Eos, Transactions American Geophysical Union, 94(34), 297-298. https://doi.org/10.1002/2013EO340001, 2013.

Li, J., Zhang, Q., Chen, Y. D., & Singh, V. P.: GCMssimulations. Eos, Transactions American Ge extremes during the 21st century in China. Journal of Geophysical Research: Atmospheres, 118(19). https://doi.org/10.1002/jgrd.50851, 2013.

Li, W., Jiang, Z., Xu, J., & Li, L.: Extreme Precipitation Indices over China in CMIP5 Models. Part II: Probabilistic Projection. Journal of Climate, 29(24), 8989-9004. https://doi.org/10.1175/JCLI-D-16-0377.1, 2016.

Li, Z., W. K.-M. Lau, V. Ramanathan et al.: Aerosol and monsoon climate interactions over Asia, *Rev. Geophys.*, 54, https://doi.org/10.1002/2015RG000500, 2016.

Lin, Z., & Wang, B.: Northern East Asian low and its impact on the interannual variation of East Asian summer rainfall. Climate dynamics, 46(1-2), 83-97. https://doi.org/10.1007/s00382-015-2570-9, 2016.

Liu, R., Liu, S. C., Cicerone, R. J., Shiu, C. J., Li, J., Wang, J., & Zhang, Y.: Trends of extreme precipitation in eastern China and their possible causes. Advances in Atmospheric Sciences, 32(8), 1027-1037. https://doi.org/10.1007/s00376-015-5002-, 2015.

Locatelli, J. D., & Hobbs, P. V.: Fall speeds and masses of solid precipitation particles. Journal of Geophysical Research, 79(15), 2185-2197. https://doi.org/10.1029/JC079i015p02185, 1974.

Lorant, V., & Royer, J. F.: Sensitivity of equatorial convection to horizontal resolution in aquaplanet simulations with a variable-resolution GCM. Monthly weather review, 129(11), 2730-2745. https://doi.org/10.1175/1520-0493(2001)129<2730:SOECTH>2.0.CO;2, 2001.

Lu, J., Chen, G., Leung, L. R., Burrows, D. A., Yang, Q., Sakaguchi, K., & Hagos, S.: Toward the dynamical convergence on the jet stream in aquaplanet AGCMs. Journal of Climate, 28(17), 6763-6782. https://doi.org/10.1175/JCLI-D-14-00761.1, 2015.

Mlawer, E. J., Taubman, S. J., Brown, P. D., Iacono, M. J., & Clough, S. A.: Radiative transfer for inhomogeneous atmospheres: RRTM, a validated correlated - k model for the longwave. Journal of Geophysical Research: Atmospheres, 102(D14), 16663-16682. https://doi.org/10.1029/97JD00237., 1997.

Molthan, A. L., & Colle, B. A.: Comparisons of single-and double-moment microphysics schemes in the simulation of a synoptic-scale snowfall event. Monthly Weather Review, 140(9), 2982-3002. https://doi.org/10.1175/MWR-D-11-00292.1, 2012.

Nakanishi, M., & Niino, H.: An improved Mellor–Yamada level-3 model: Its numerical stability and application to a regional prediction of advection fog. Boundary-Layer Meteorology, 119(2), 397-407. https://doi.org/10.1007/s10546-005-9030-8, 2006.

Nakanishi, M., & Niino, H.: Development of an improved turbulence closure model for the atmospheric boundary layer. Journal of the Meteorological Society of Japan. Ser. II, 87(5), 895-912. https://doi.org/10.2151/jmsj.87.895, 2009.

NRC: National Research Council Board, A National Strategy for Advancing Climate Modeli ng, The National Academies Press, Washington, DC (2012) (http://www.nap.edu/cata log/13430/a-national-strategy-for-advancing-climate-modeling, last access: April 25, 2019).

O'Brien, T. A., Collins, W. D., Kashinath, K., Rübel, O., Byna, S., Gu, J., Krishnan, H, Ullrich, P.: Resolution dependence of precipitation statistical fidelity in hindcast simulations. Journal of Advances in Modeling Earth Systems, 8(2), 976-990. https://doi.org/10.1002/2016MS000671, 2016.

O'Brien, T. A., Li, F., Collins, W. D., Rauscher, S. A., Ringler, T. D., Taylor, M., Hagos, S. M., Leung, L. R.: Observed scaling in clouds and precipitation and scale incognizance in regional to global atmospheric models. Journal of Climate, 26(23), 9313-9333. https://doi.org/10.1175/JCLI-D-13-00005.1, 2013.

964 Park, S. H., Skamarock, W. C., Klemp, J. B., Fowler, L. D., & Duda, M. G.: Evaluation of
965 global atmospheric solvers using extensions of the Jablonowski and Williamson
966 baroclinic wave test case. Monthly Weather Review, 141(9), 3116-3129.
967 https://doi.org/10.1175/MWR-D-12-00096.1, 2013.
968 Pedersen, C. A., & Winther, J. G.: Intercomparison and validation of snow albedo
969 parameterization schemes in climate models. Climate Dynamics, 25(4), 351-362:
970 https://doi.org/10.1007/s00382-005-0037-0, 2005.
971 Prein, A. F., Langhans, W., Fosser, G., Ferrone, A., Ban, N., Goergen, K., ... & Brisson, E.: A
972 review on regional convection - permitting climate modeling: Demonstrations,
973 prospects, and challenges. Reviews of geophysics, 53(2), 323-361.
974 https://doi.org/10.1002/2014RG000475, 2015.
975 Prein, A. F., Rasmussen, R. M., Ikeda, K., Liu, C., Clark, M. P., & Holland, G. J.: The future
976 intensification of hourly precipitation extremes. Nature Climate Change, 7(1), 48.
977 https://doi.org/10.1038/nclimate3168, 2017.
978 Rauscher, S. A., O'Brien, T. A., Piani, C., Coppola, E., Giorgi, F., Collins, W. D., & Lawston,
979 P. M.: A multimodel intercomparison of resolution effects on precipitation: simulations
980 and theory. Climate dynamics, 47(7-8), 2205-2218. https://doi.org/10.1007/s00382-
981 015-2959-5, 2016.
982 Rauscher, S. A., Ringler, T. D., Skamarock, W. C., & Mirin, A. A.: Exploring a global
983 multiresolution modeling approach using aquaplanet simulations. Journal of
984 Climate, 26(8), 2432-2452. https://doi.org/10.1175/JCLI-D-12-00154.1, 2013.
985 Rhoades, A. M., Huang, X., Ullrich, P. A., & Zarzycki, C. M.: Characterizing Sierra Nevada
986 snowpack using variable-resolution CESM. Journal of Applied Meteorology and
987 Climatology, 55(1), 173-196. https://doi.org/10.1175/JAMC-D-15-0156.1, 2016.
988 Rhoades, A. M., Ullrich, P. A., Zarzycki, C. M., Johansen, H., Margulis, S. A., Morrison, H., ...
989 & Collins, W. D.: Sensitivity of Mountain Hydroclimate Simulations in Variable -
990 Resolution CESM to Microphysics and Horizontal Resolution. Journal of Advances in
991 Modeling Earth Systems, 10(6), 1357-1380. https://doi.org/10.1029/2018MS001326,
992 2018.
993 Ringler, T. D., Jacobsen, D., Gunzburger, M., Ju, L., Duda, M., & Skamarock, W.: Exploring
994 a multiresolution modeling approach within the shallow-water equations. Monthly
995 Weather Review, 139(11), 3348-3368. https://doi.org/10.1175/MWR-D-10-05049.1,
996 2011.

997 Ringler, T., Ju, L., & Gunzburger, M.: A multiresolution method for climate system modeling:
998 Application of spherical centroidal Voronoi tessellations. Ocean Dynamics, 58(5-6),
999 475-498. https://doi.org/10.1007/s10236-008-0157-2, 2008.
1000 Sakaguchi, K., Leung, L. R., Zhao, C., Yang, Q., Lu, J., Hagos, S.: Exploring a multiresolution
1001 approach using AMIP simulations. Journal of Climate, 28(14), 5549-5574.
1002 https://doi.org/10.1175/JCLI-D-14-00729.1, 2015.
1003 Sakaguchi, K., Lu, J., Leung, L. R., Zhao, C., Li, Y., & Hagos, S.: Sources and pathways of
1004 the upscale effects on the Southern Hemisphere jet in
1005 MPASs. s. ions. s. ons. ultiresolution approach using AMIP simulations. lations. nd
1006 Williams25-10431043 4(6https://doi.org/10.1002/2016MS000743, 2016.
1007 Skamarock, W. C., & Gassmann, A.: Conservative transport schemes for spherical geodesic
1008 grids: High-order flux operators for ODE-based time integration. Monthly Weather
1009 Review, 139(9), 2962-2975. https://doi.org/10.1175/MWR-D-10-05056.1, 2011.
1010 Skamarock, W. C., & Klemp, J. B.: A time-split nonhydrostatic atmospheric model for weather
1011 research and forecasting applications. Journal of Computational Physics, 227(7), 3465-
1012 3485. https://doi.org/10.1016/j.jcp.2007.01.037, 2008.
1013 Skamarock, W. C., Klemp, J. B., Duda, M. G., Fowler, L. D., Park, S. H., & Ringler, T. D.: A
1014 multiscale nonhydrostatic atmospheric model using centroidal Voronoi tesselations and
1015 C-grid staggering. Monthly Weather Review, 140(9), 3090-3105.
1016 https://doi.org/10.1175/MWR-D-11-00215.1, 2012.
1017 Sukovich, E. M., Ralph, F. M., Barthold, F. E., Reynolds, D. W., & Novak, D. R.: Extreme
1018 quantitative precipitation forecast performance at the Weather Prediction Center from
1019 2001 to 2011. Weather and Forecasting, 29(4), 894-911. https://doi.org/10.1175/WAF-
1020 D-13-00061.1, 2014.
1021 Thompson, G., Field, P. R., Rasmussen, R. M., & Hall, W. D.: Explicit forecasts of winter
1022 precipitation using an improved bulk microphysics scheme. Part II: Implementation of
1023 a new snow parameterization. Monthly Weather Review, 136(12), 5095-5115.
1024 https://doi.org/10.1175/2008MWR2387.1, 2008.
1025 Wang, M., & Ullrich, P.: Marine air penetration in California's Central Valley: Meteorological
1026 drivers and the impact of climate change. Journal of Applied Meteorology and
1027 Climatology, 57(1), 137-154. https://doi.org/10.1175/JAMC-D-17-0089.1, 2018.
1028 Wang, Y., Leung, L. R., McGREGOR, J. L., Lee, D. K., Wang, W. C., Ding, Y., & Kimura,
1029 F.: Regional climate modeling: progress, challenges, and prospects. Journal of the

1030 Meteorological Society of Japan. Ser. II, 82(6), 1599-1628.
1031 https://doi.org/10.2151/jmsj.82.1599, 2004.
1032 Wicker, L. J., & Skamarock, W. C.: Time-splitting methods for elastic models using forward
1033 time schemes. Monthly weather review, 130(8), 2088-2097.
1034 https://doi.org/10.1175/1520-0493(2002)130<2088:TSMFEM>2.0.CO;2, 2002.
1035 Wu, C., Liu, X., Lin, Z., Rhoades, A. M., Ullrich, P. A., Zarzycki, C. M., ... & Rahimi-Esfarjani,
1036 S. R.: Exploring a variable-resolution approach for simulating regional climate in the
1037 Rocky Mountain region using the VR-CESM. Journal of Geophysical Research:
1038 Atmospheres, 122(20), 10-939. https://doi.org/10.1002/2017JD027008, 2017.
1039 Xiang, S., Li, Y., Li, D., & Yang, S.: An analysis of heavy precipitation caused by a retracing
1040 plateau vortex based on TRMM data. Meteorology and Atmospheric Physics, 122(1-2),
1041 33-45. https://doi.org/10.1007/s00703-013-0269-1, 2013.
1042 Xu, H., & Yao, W.: A numerical study of the Beijing extreme rainfall of 21 July 2012 and the
1043 impact of topography. Advances in Meteorology, 2015.
1044 http://dx.doi.org/10.1155/2015/980747, 2015.
1045 Xue, M., Kong, F., Weber, D., Thomas, K. W., Wang, Y., Brewster, K., ... & Coniglio, M. C.:
1046 CAPS realtime storm-scale ensemble and high-resolution forecasts as part of the
1047 NOAA Hazardous Weather Testbed 2007 spring experiment. In 22nd Conf. Wea. Anal.
1048 Forecasting/18th Conf. Num. Wea. Pred, 2007.
1049 Xu, Z., Rhoades, A. M., Johansen, H., Ullrich, P. A., & Collins, W. D.: An intercomparison of
1050 GCM and RCM dynamical downscaling for characterizing the hydroclimatology of
1051 California and Nevada. Journal of Hydrometeorology, 19(9), 1485-1506.
1052 https://doi.org/10.1175/JHM-D-17-0181.1, 2018.
1053 Yang, Q., Leung, L. R., Rauscher, S. A., Ringler, T. D., & Taylor, M. A.: Atmospheric moisture
1054 budget and spatial resolution dependence of precipitation extremes in aquaplanet
1055 simulations. Journal of Climate, 27(10), 3565-3581. https://doi.org/10.1175/JCLI-D-
1056 13-00468.1, 2014.
1057 Yang, Q., R. Houze, Jr., L.R. Leung, & Z. Feng : Environments of long-lived mesoscale
1058 convective systems over the Central United States in convection permitting climate
1059 simulations. J. Geophys. Res., 122, https://doi.org/10.1002/2017JD027033, 2017.
1060 Yao, X. P., Sun, J. Y., & Ma J. L.: Advances on research of Yangtze-Huaihe shear line. Plateau
1061 Meteorology, 36(4), 1138-1151 (in Chinese), 2017.

1062 Yessad, K., & Bénard, P.: Introduction of a local mapping factor in the spectral part of the
1063 Météo-France global variable mesh numerical forecast model. Quarterly Journal of the
1064 Royal Meteorological Society, 122(535), 1701-1719.
1065 https://doi.org/10.1002/qj.49712253511, 1996.
1066 Zarzycki, C. M., Jablonowski, C., & Taylor, M. A.: Using variable resolution meshes to model
1067 tropical cyclones in the community atmosphere model. Monthly Weather Review,
1068 142(3), 1221–1239. https://doi.org/10.1175/MWR-D-13-00179.1, 2014.
1069 Zarzycki CM, Jablonowski C, Thatcher DR, Taylor MA: Effects of localized grid refinement
1070 on the general circulation and climatology in the community atmosphere model. J Clim
1071 28:2777–2803. https://doi.org/10.1175/JCLI-D-14-00599.1, 2015.
1072 Zhang, D. L., Lin, Y., Zhao, P., Yu, X., Wang, S., Kang, H., & Ding, Y.: The Beijing extreme
1073 rainfall of 21 July 2012:"Right results" but for wrong reasons. Geophysical Research
1074 Letters, 40(7), 1426-1431. https://doi.org/10.1002/grl.50304, 2013.
1075 Zhang, H., & Zhai, P.: Temporal and spatial characteristics of extreme hourly precipitation
1076 over eastern China in the warm season. Advances in atmospheric sciences, 28(5), 1177.
1077 https://doi.org/10.1007/s00376-011-0020-0, 2011.
1078 Zhang, L., Dong, M., & Wu, T.: Changes in precipitation extremes over eastern China
1079 simulated by the Beijing Climate Center Climate System Model (BCC_CSM1.
1080 0). Climate Research, 50(2-3), 227-245. https://doi.org/10.3354/cr01066, 2011.
1081 Zhang, Q., Xiao, M., Singh, V. P., Liu, L., & Xu, C. Y.: Observational evidence of summer
1082 precipitation deficit-temperature coupling in China. Journal of Geophysical Research:
1083 Atmospheres, 120(19). https://doi.org/10.1002/2015JD023830, 2011.
1084 Zhang, Q., Zheng, Y., Singh, V. P., Luo, M., & Xie, Z.: Summer extreme precipitation in
1085 eastern China: Mechanisms and impacts. Journal of Geophysical Research:
1086 Atmospheres, 122(5), 2766-2778. https://doi.org/10.1002/2016JD025913, 2017.
1087 Zhang,Y., P., L., & Zhong, Q.: An interdecadal change in the relationship between the western
1088 North Pacific Ocean and the East Asian summer monsoon. Climate Dynamics, 49(4),
1089 1139-1156. https://doi.org/10.1007/s00382-016-3370-6, 2017.
1090 Zhai, P., Zhang, X., Wan, H., & Pan, X.: Trends in total precipitation and frequency of daily
1091 precipitation extremes over China. Journal of Climate, 18(7), 1096-1108.
1092 https://doi.org/10.1175/JCLI-3318.1, 2005.
1093 Zhao, C., Leung, L. R., Park, S. H., Hagos, S., Lu, J., Sakaguchi, K., ... & Duda, M. G.:
1094 Exploring the impacts of physics and resolution on aqua,planet simulations from a

nonhydrostatic global variablemresolution modeling framework. Journal of Advances in Modeling Earth Systems, 8(4), 1751-1768. https://doi.org/10.1002/2016MS000727, 2017.

Zhao, Y., Xu, X., Zhao, T., Xu, H., Mao, F., Sun, H., & Wang, Y.: Extreme precipitation events in East China and associated moisture transport pathways. Science China Earth Sciences, 59(9), 1854-1872. https://doi.org/10.1007/s11430-016-5315-7, 2016.

Zheng, Y., Xue, M., Li, B., Chen, J., & Tao, Z.: Spatial characteristics of extreme rainfall over China with hourly through 24-hour accumulation periods based on national-level hourly rain gauge data. Advances in Atmospheric Sciences, 33(11), 1218-1232. https://doi.org/10.1007/s00376-016-6128-5, 2016.

Zhong, S., pQian, Y., Zhao, C., Leung, R., & Yang, X. Q.: A case study of urbanization impact on summer preciitation in the Greater Beijing Metropolitan Area: Urban heat island versus aerosol effects. Journal of Geophysical Research: Atmospheres, 120(20), 10-903. https://doi.org/10.1002/2015JD023753, 2015.

Zhong, S., Qian, Y., Zhao, C., Leung, R., Wang, H., Yang, B., ... & Liu, D.: Urbanization-induced urban heat island and aerosol effects on climate extremes in the Yangtze River Delta region of China. Atmospheric Chemistry and Physics, 17(8), 5439-5457. https://doi.org/10.5194/acp-17-5439-2017, 2017.

Zhou, T. J., & Li, Z.: Simulation of the East Asian summer monsoon using a variable resolution atmospheric GCM. Climate Dynamics, 19(2), 167-180. https://doi.org/10.1007/s00382-001-0214-8, 2002.

Table 1 Numerical Experiments conducted and analyzed in this study

Physics/Resolution	MPAS				
	U15km	U60km	V30km	V16km	V4km
WSM6+NTD	Yes	/	/	Yes	/
WSM6+GF	Yes	Yes	Yes	Yes	Yes
Thompson+GF	/	/	/	/	Yes

(1) 'U' and 'V' represent quasi-uniform and variable resolution meshes, respectively, as described in the Section 2.1.2.
(2) 'WSM6' and 'Thompson' represent two cloud microphysics schemes as described in the Section 2.1.1; 'NTD' and 'GF' represent two cumulus parameterizations as described in the Section 2.1.1.

Table 2 The correlation coefficients and the corresponding 95% confidence intervals based on the bootstrap analysis for the results shown in Fig. 6-10

	GFS.1deg	GFS.0.5deg	U60km.WSM6	V30km.WSM6	V16km.WSM6	V4km.WSM6	V4km.Thompson
Fig. 6	0.06 (0.006~0.1)	0.03 (-0.01~0.08)	0.49 (0.45~0.54)	0.47 (0.43~0.53)	0.56 (0.50~0.61)	0.63 (0.54~0.67)	0.54 (0.48~0.59)
Fig. 7	-0.15 (-0.35~0.24)	-0.19 (-0.39~0.15)	0.68 (0.49~0.84)	0.71 (0.46~0.88)	0.89 (0.78~0.95)	0.97 (0.93~0.99)	0.72 (0.45~0.93)
Fig. 8	0.03 (-0.02~0.09)	0.02 (-0.03~0.08)	0.30 (0.25~0.37)	0.32 (0.27~0.41)	0.41 (0.37~0.48)	0.42 (0.39~0.49)	0.38 (0.32~0.44)
Fig. 9	0.32 (0.23~0.41)	0.29 (0.20~0.41)	0.53 (0.45~0.61)	0.68 (0.64~0.72)	0.80 (0.77~0.83)	0.85 (0.82~0.88)	0.80 (0.75~0.84)
Fig. 10	/	/	0.20 (0.13~0.28)	0.21 (0.12~0.30)	0.30 (0.19~0.40)	0.50 (0.39~0.59)	0.42 (0.34~0.51)

(1) The values inside the parenthesis indicate the lower and higher bounds of 95% confidence intervals; the values outside are estimated directly based on the results shown in Fig. 6-10.

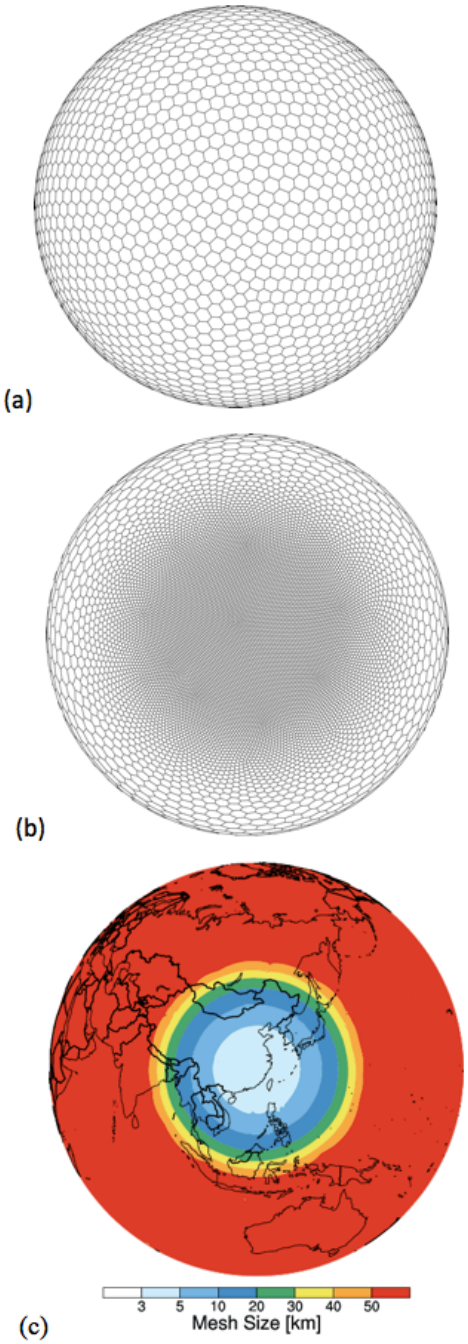

Figure 1 (a) quasi-uniform mesh and (b) variable-resolution mesh used in the MPAS experiments. Both meshes are plotted at resolutions significantly lower than used in the experiments to show the mesh cells. (c) global variable-resolution mesh size distribution in the variable resolution 4-60 km experiment.

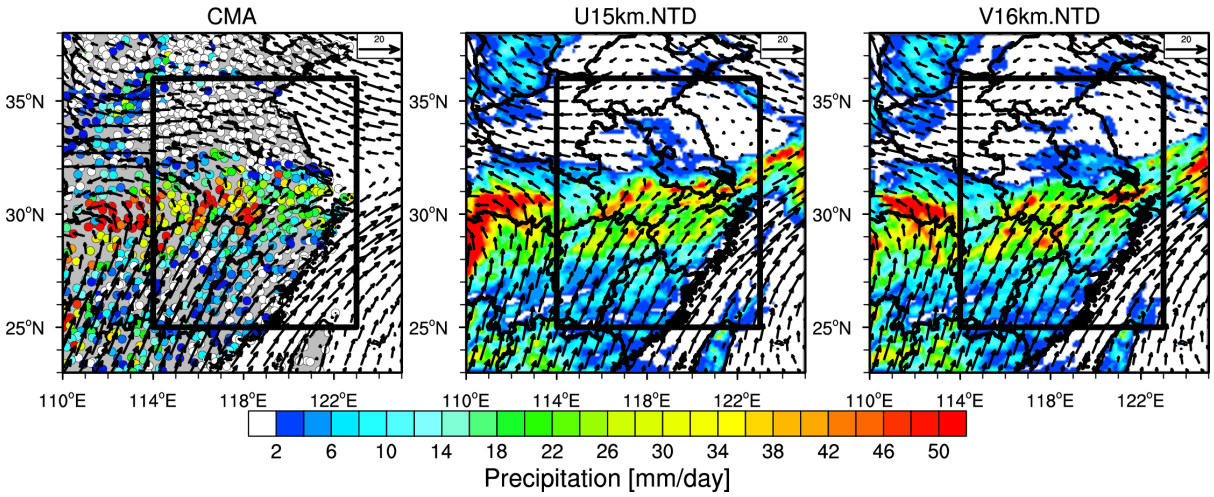

Figure 2 Spatial distributions of precipitation and wind fields at 850 hPa averaged during the event (June 25 00:00 to June 27 12:00 UTC time) from the simulations with the global uniform (15 km) and variable (16 km over the refined region as shown in Fig. 1c) resolutions. The observed mean precipitation from the CMA stations and the wind fields from the ERA5 reanalysis are shown. The black box denotes the region for the analysis in the following.

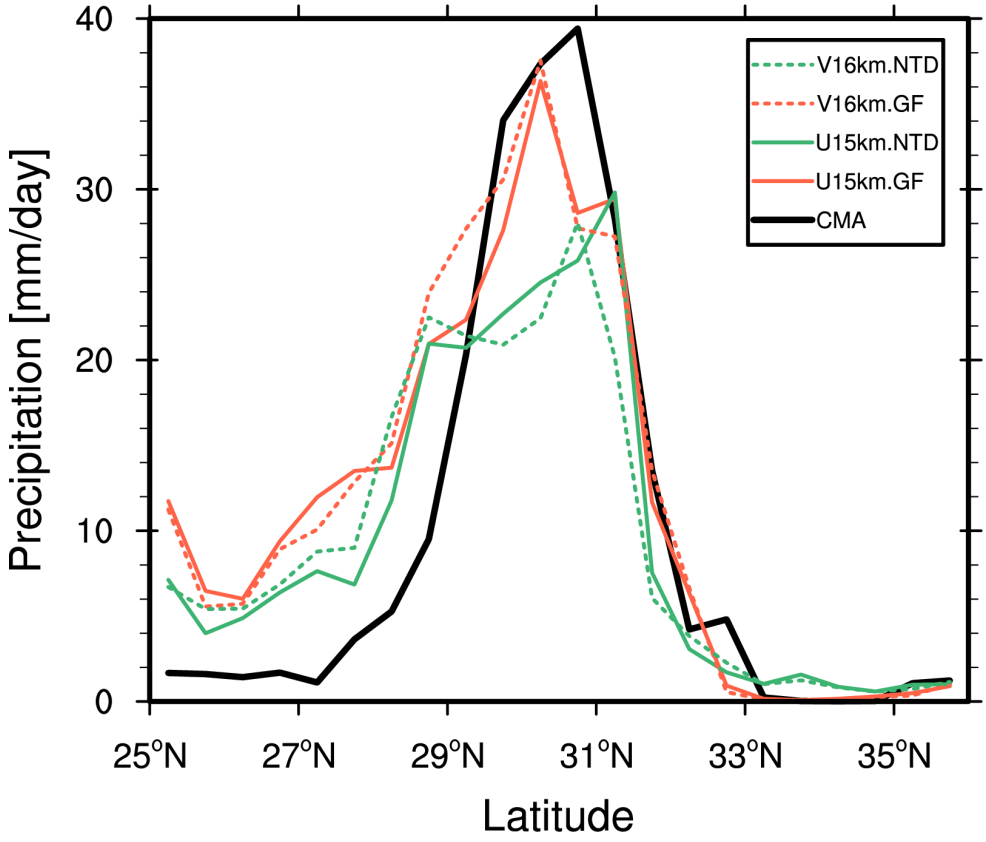

Figure 3 Zonal distributions of precipitation averaged during the event (June 25 00:00 to June 27 12:00 UTC time) over East China (denoted as the black box in Fig. 2) from the CMA station observations and the simulations with the global uniform (15 km, solid lines) and variable (16 km over the refined region as shown in Fig. 1c, dash lines) resolutions with two convective parameterizations (GF, red lines; NTD, green lines). The modeling results are sampled at the CMA station.

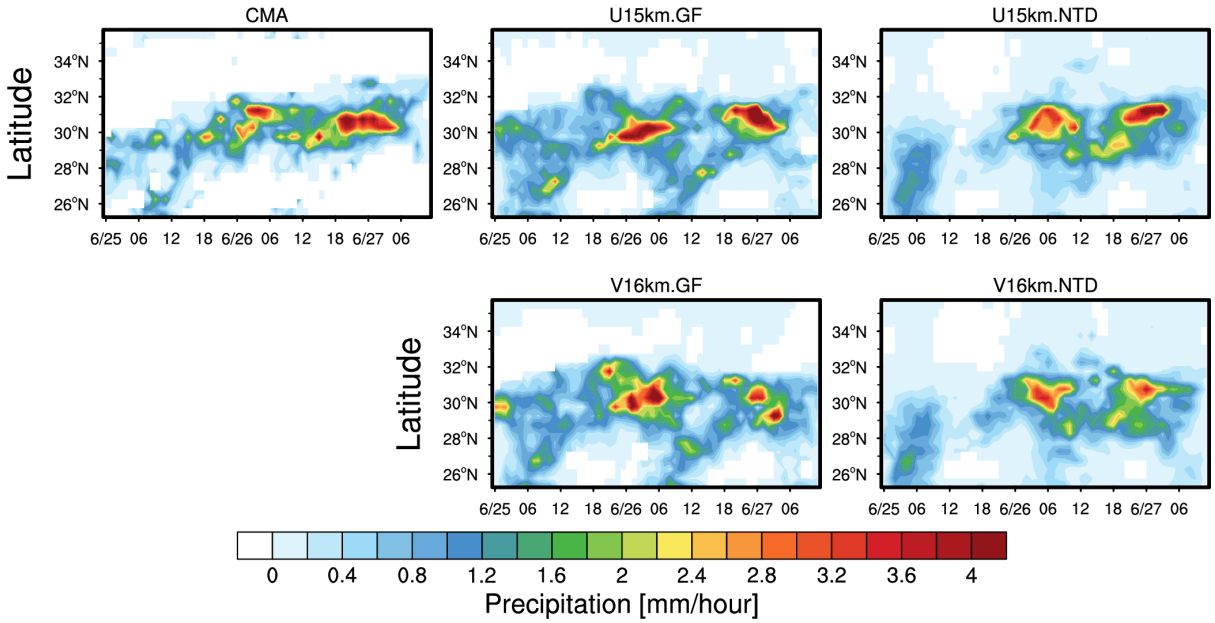

Figure 4 Time-Latitude cross section of precipitation during the event over East China from the CMA station observations and the simulations with the global uniform and variable resolutions with two convective parameterizations. The modeling results are sampled at the CMA stations.

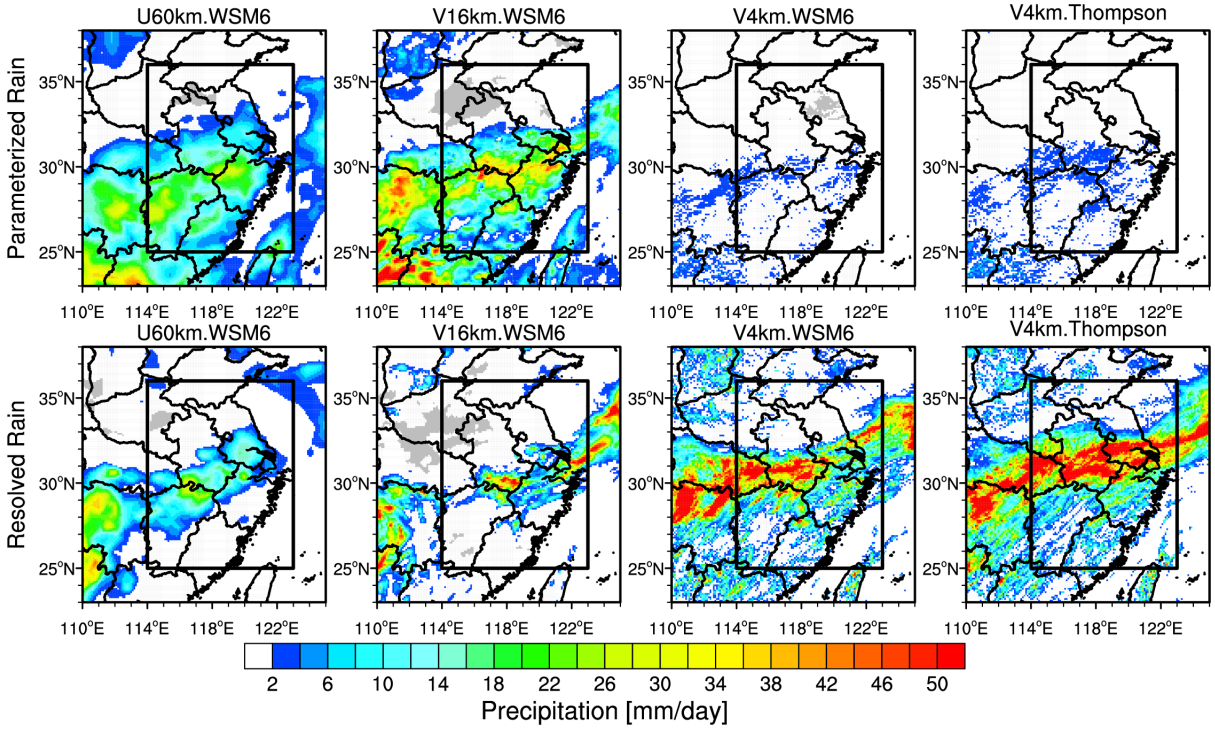

Figure 5 Spatial distribution of averaged parameterized and resolved precipitation during the event over East China from the simulations with the resolutions of 60 km, 16 km, and 4 km.

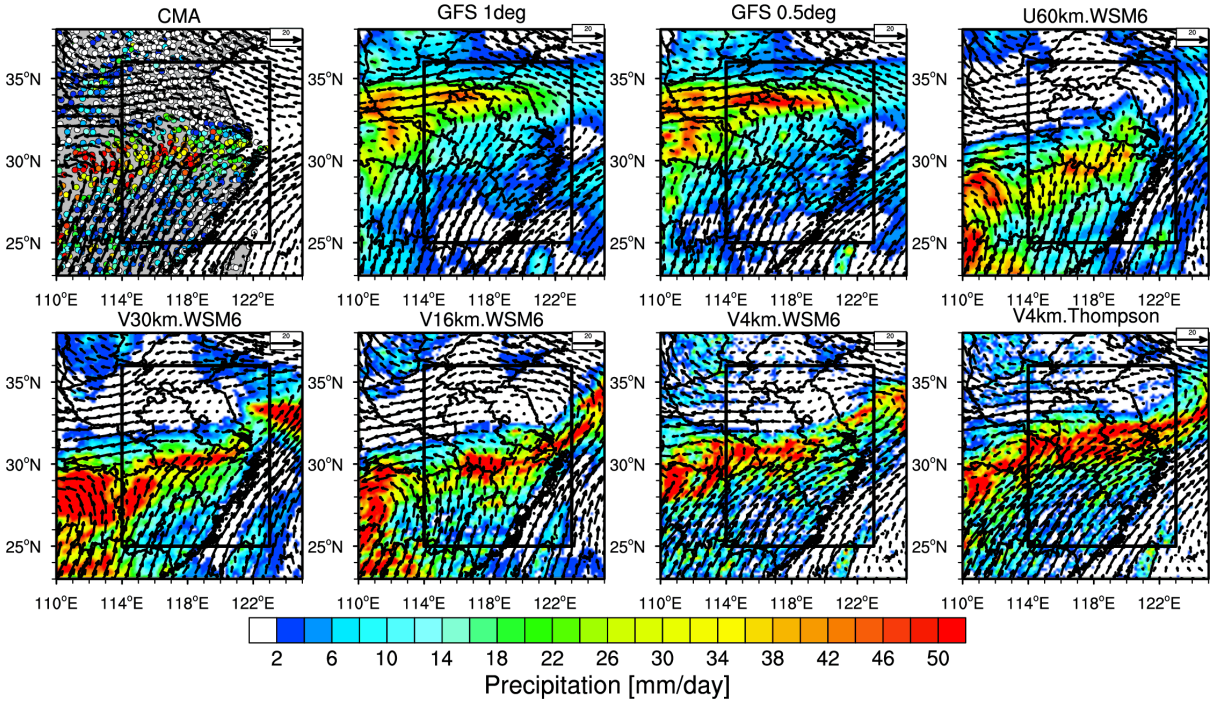

Figure 6 Spatial distributions of precipitation and wind fields at 850 hPa averaged during the event from the MPAS simulations at the resolutions of 60 km, 30 km, 16 km, and 4 km. The observed mean precipitation from the CMA stations and the wind fields from the ERA5 reanalysis are shown as well. The black box denotes the region for the analysis in the following. For comparison, the GFS forecasts at 1 degree and 0.5 degree resolutions are also shown.

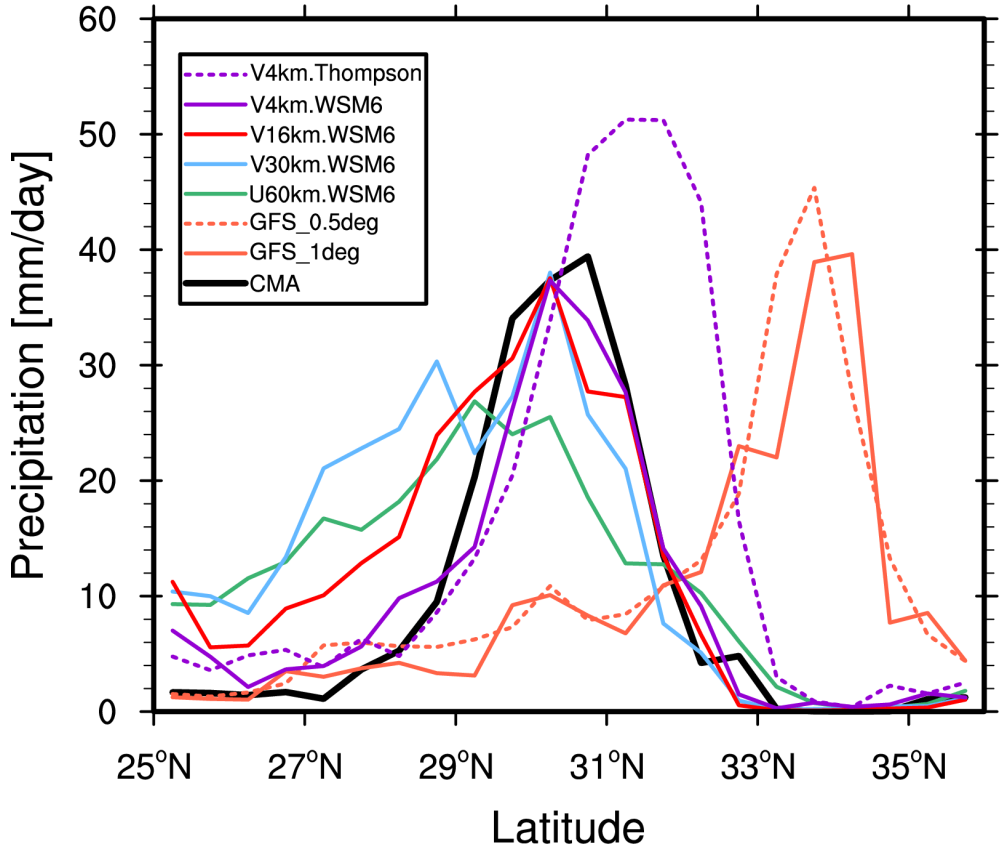

Figure 7 Zonal distributions of precipitation averaged during the event over East China from the CMA station observations and the simulations with the resolutions of 60 km, 30 km, 16 km, and 4 km. For comparison, the GFS forecasts at 1 degree and 0.5 degree resolutions are also included. The modeling results are sampled at the CMA stations.

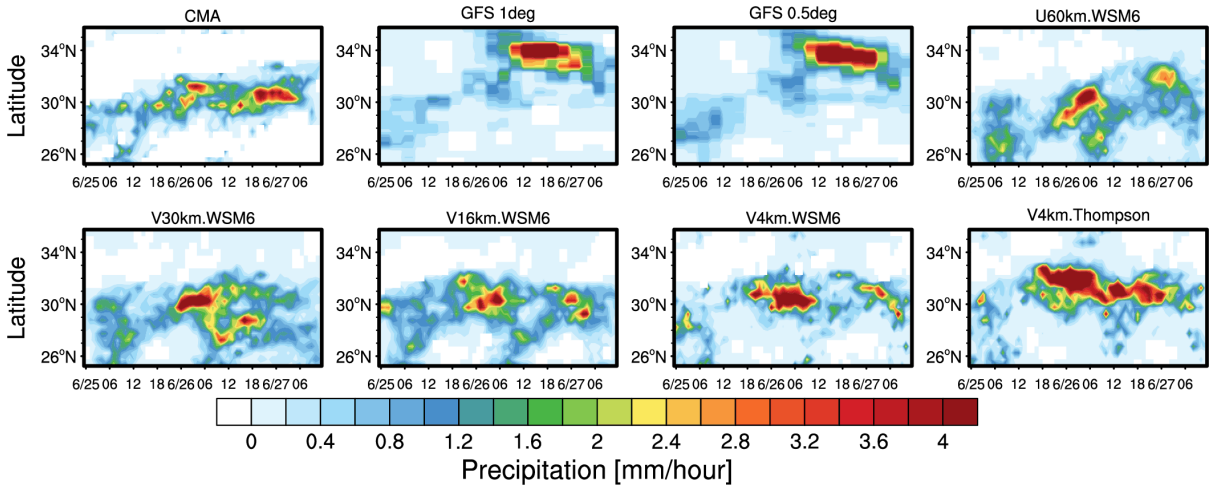

Figure 8 Time-Latitude cross section of precipitation during the event over East China from the CMA station observations, GFS forecasts at 0.5° and 1.0° resolutions, and the MPAS simulations at resolutions of 60 km, 30 km, 16 km, and 4 km over East China. The simulations at 4 km are with two cloud microphysics schemes (WSM6 and Thompson). The modeling results are sampled at the CMA stations.

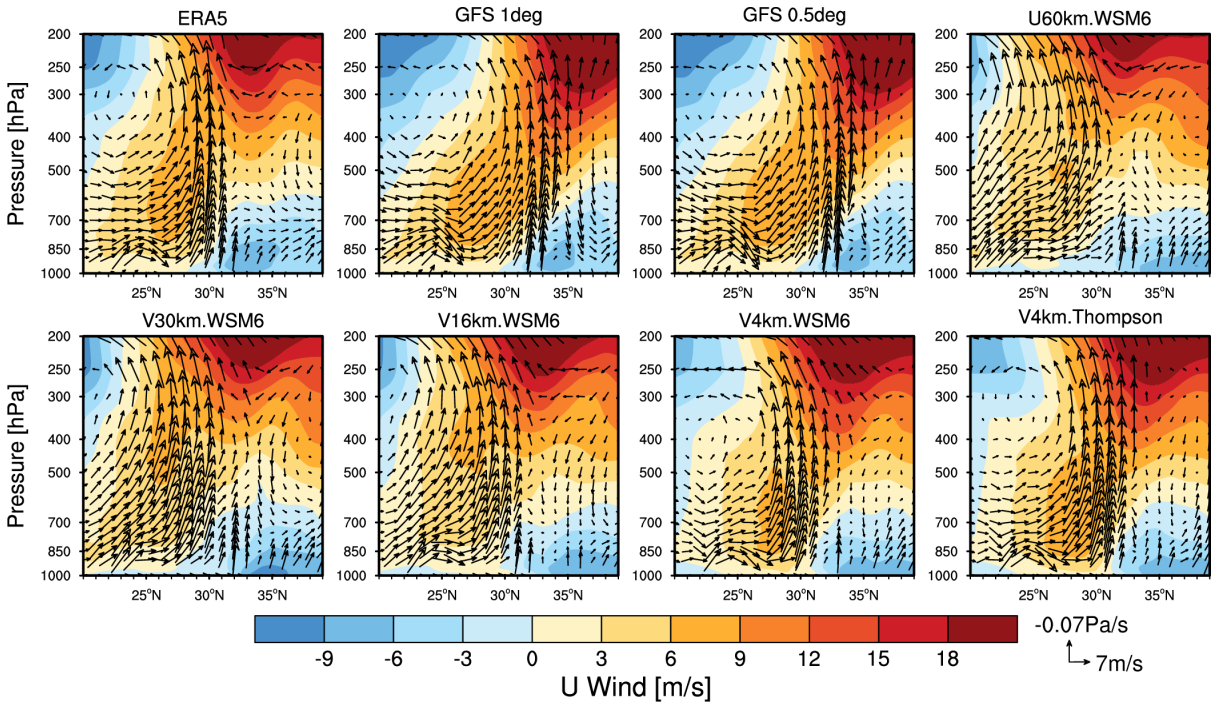

Figure 9 Height-Latitude cross section of wind fields averaged over the region (as shown in Fig. 6) during the event from the ERA-interim reanalysis, the GFS forecasts at 0.5° and 1.0° resolutions, and the MPAS simulations at resolutions of 60 km, 30 km, 16 km, and 4 km. The simulations at 4 km are with two cloud microphysics schemes (WSM6 and Thompson). The positive color represents eastward wind. All the datasets are regridded into 0.25° horizontal resolution.

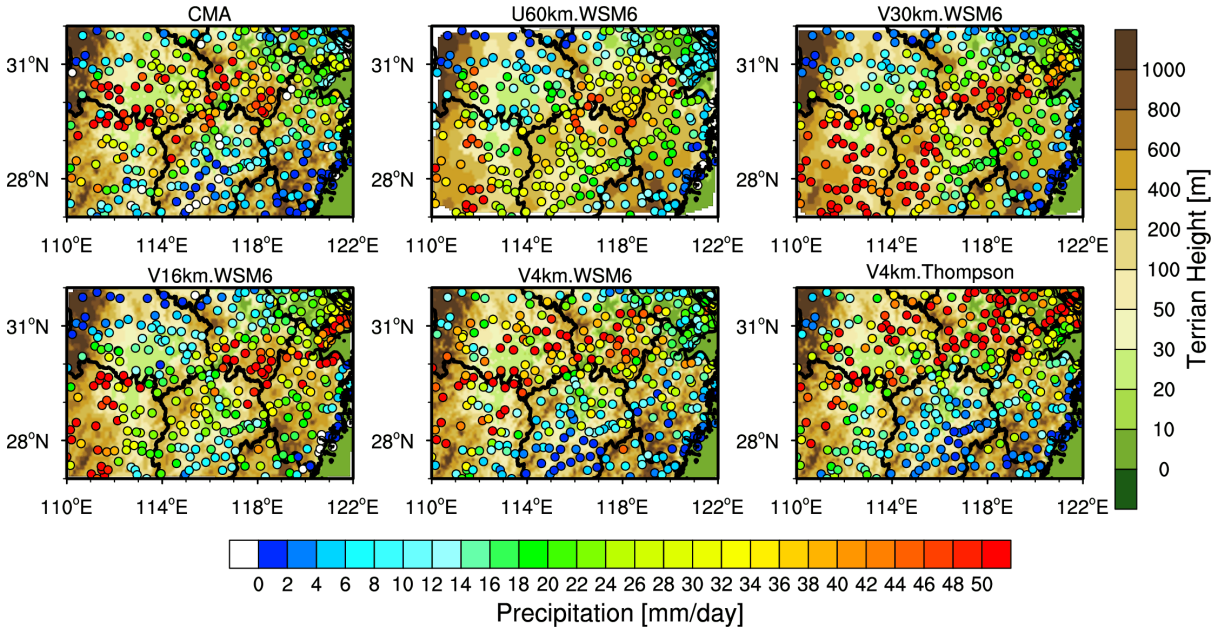

Figure 10 Spatial distributions of precipitation averaged during the event over the heavy precipitation region (27°N-32°N and 110°E-122°E) from the CMA observations and the MPAS simulations at the resolutions of 60 km, 30 km, 16 km, and 4 km. The simulations are sampled at the CMA stations. The topography is also shown.

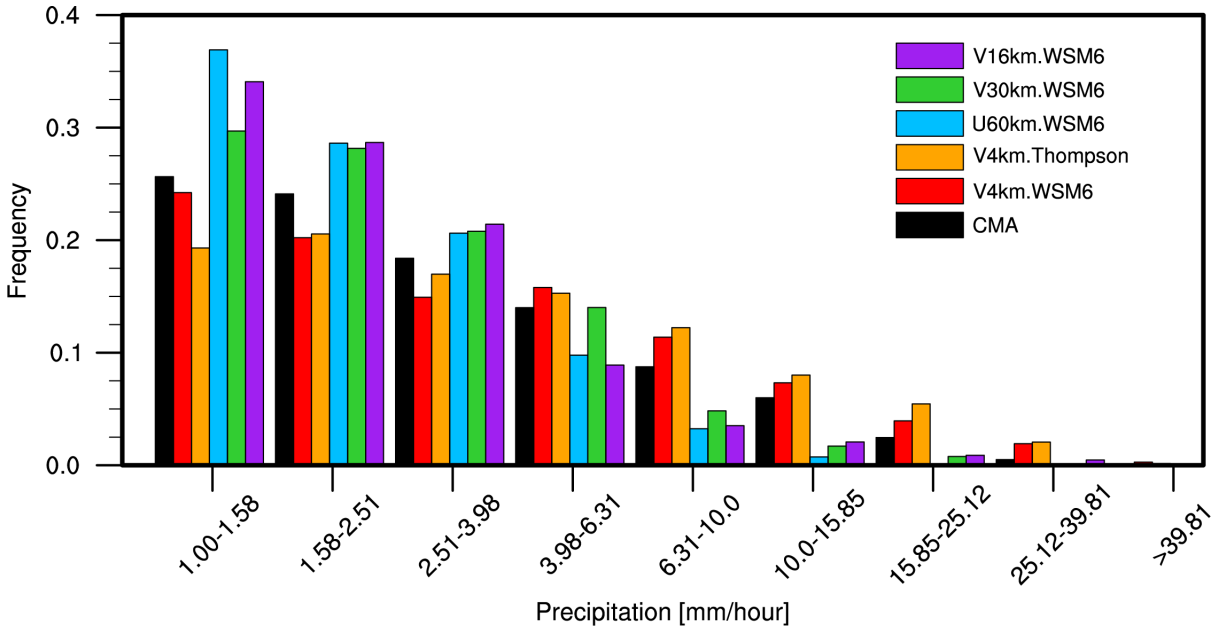

Figure 11 Probability density functions (PDFs) of hourly precipitation at all the CMA stations during the event over East China from the CMA observations and the MPAS simulations at the resolutions of 60 km, 30 km, 16 km, and 4 km. The simulations are sampled at the CMA stations.

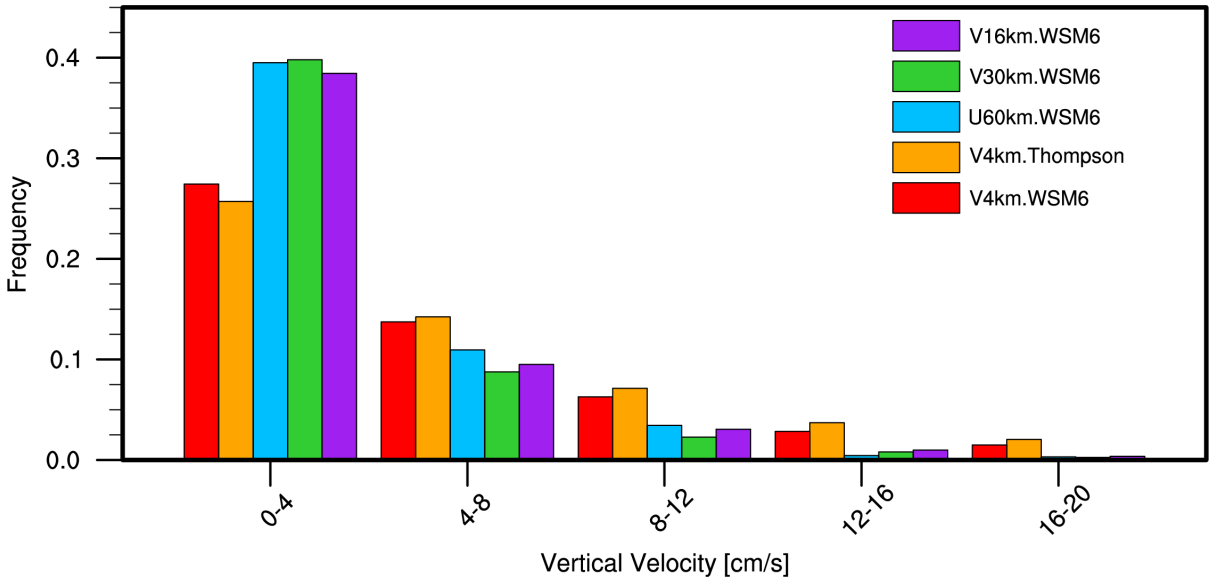

Figure 12 Probability density functions (PDFs) of hourly upward vertical velocity averaged below 700 hPa at all the CMA stations during the event over East China from the MPAS simulations at the resolutions of 60 km, 30 km, 16 km, and 4 km.

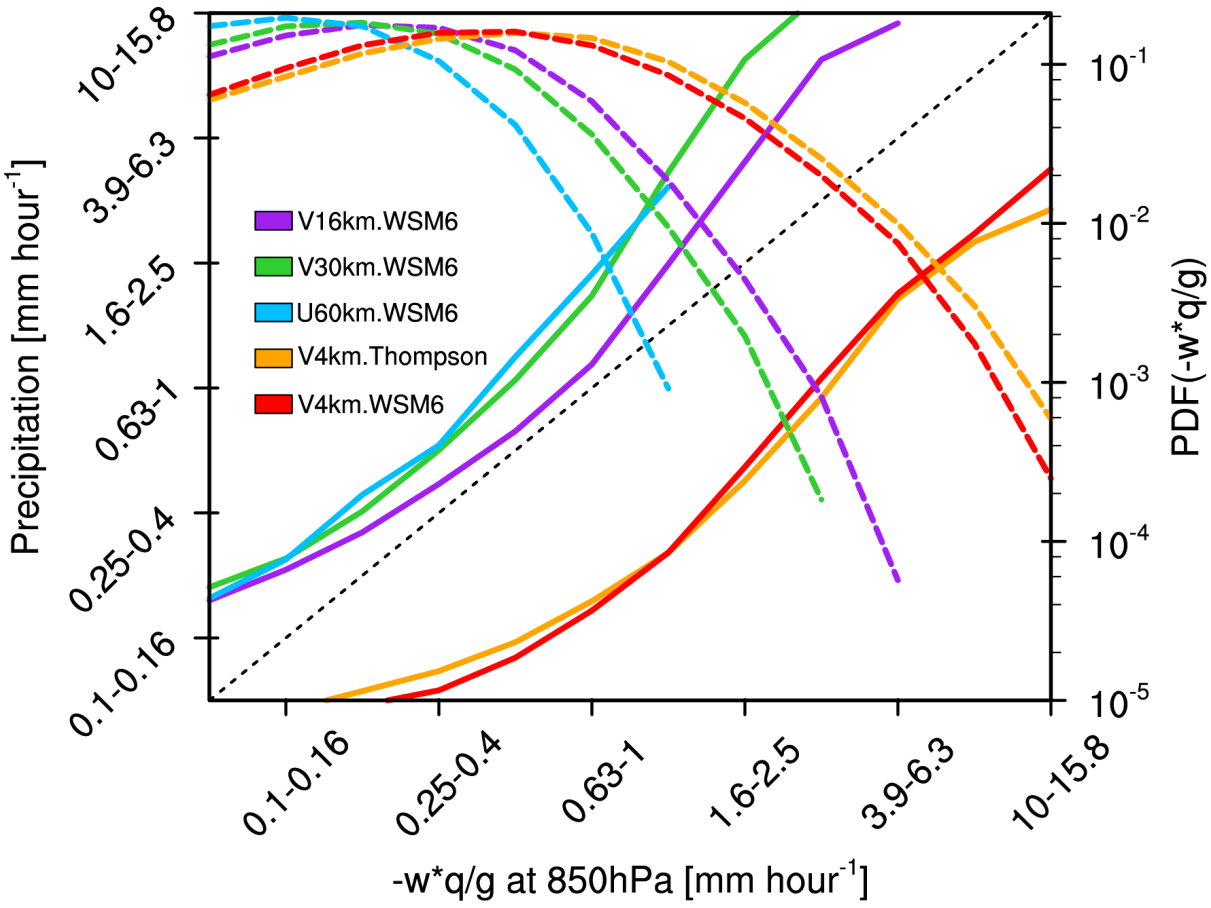

Figure 13 Hourly precipitation versus upward moisture flux at 850hPa during the event over East China from the MPAS simulations at the resolution of 60km, 30km, 16km and 4km (solid line, left axis), and the PDFs of the upward moisture flux (dash line, right axis).